Multi-annual embayment sediment dynamics involving headland bypassing and sediment exchange across the depth of closure

Nieves G. Valiente[1], Robert Jak McCarroll[1], Gerd Masselink[1], Tim Scott[1], Mark Wiggins[1]

[1]School of Biological and Marine Sciences, University of Plymouth, PL4 8AA, UK

Corresponding author: Nieves G. Valiente (nieves.garciavaliente@plymouth.ac.uk)

https://doi.org/10.1016/j.geomorph.2019.06.020

Keywords:

Storm response, sediment budget, beach recovery, sediment dynamics, nearshore sediment transport, beach morphodynamics

Highlights:

- Full sediment budget was produced along an exposed macrotidal embayment and linked to wave forcing
- Inter- and sub-tidal volume are not inversely correlated, indicating decoupling
- Sediment budget suggests significant exchange around headlands and/or across depth of closure
- Beaches on this coast type can be considered part of an extended coastal cell

Abstract

Predicting the future behavior of beach and nearshore systems requires an accurate delineation and understanding of coastal cell boundaries, sediment transport pathways, and sediment sources and sinks. Unfortunately, there is a paucity of field datasets on beach and nearshore morphological change that extend fully from the top of the dunes to beyond the depth of closure to enable quantification of the sediment budget. Here, for the first time, we employ a total sediment budget approach, examining a sandy and embayed beach located in the north coast of SW England, to investigate inter- and multi-annual embayment scale sediment dynamics over a 10-year period that includes extreme storm erosion and post-storm recovery. We demonstrate that, despite the deeply embayed nature of the beach, the shoreline orientation roughly parallel to the dominant wave direction and the overwhelmingly cross-shore forcing of the inter-tidal beach volume, the system is neither closed, nor balanced. The very significant net changes in the recorded sediment volume from dune top to depth of closure (-14.5 m ODN), representing a loss of c. 100 m3 m-1 during the extreme storm period and a gain of c. 200 m3 m-1 during the recovery period, indicate that significant sediment transport occurs seaward of the base of the terminating headlands and beyond the morphological depth of closure. The results further indicate that the inter-tidal region is partly uncoupled from the sub-tidal region, with the former region dominated by cross-shore sediment fluxes, whereas the subtidal region is also significantly affected by longshore sediment fluxes. A conceptual model is presented that balances the observed volume changes with inferred fluxes, forced by variations in total and alongshore wave power. This study contradicts the general assumption that when sediment exits the inter-tidal, it rests undisturbed in the sub-tidal, waiting for a period of low-moderate energy to bring it onshore. The large sediment volumetric variations across the lower shoreface (depth of 5–20 m), which are of the same order of magnitude as, but uncorrelated with, those occurring in the inter-tidal region, are suggestive of an energetic longshore transport system across this deeper region. It is possible that this transport system extends along the whole north coast of SW England and this finding may lead to a shift in understanding of sediment budgets along exposed and macrotidal embayments globally.

1. Introduction

Sandy beaches and coastal dunes have significant natural capital through representing efficient and natural coastal defenses that can protect the hinterland from coastal flooding. In a context of increasing winter-wave conditions (Castelle et al., 2018) and rate of sea-level rise (Church and White, 2011), it is important to understand how coasts respond and evolve as a result of changing boundary conditions, as this significantly affects continued human occupation of the coastal zone. Predicting coastal system behavior requires an accurate delineation and understanding of coastal cell boundaries, sediment sources and sinks, and transport pathways. The difficulties with identifying these key sediment-related factors, attributed to large uncertainties associated with sediment transport modelling and a paucity of high-quality field datasets extending from the top of the dunes to depths beyond the depth of closure (Aagaard, 2011; Coco et al., 2014), inhibit accurate quantification of sediment fluxes in a particular littoral cell. Moreover, long-term beach response is controlled by the sediment exchanges between the different beach sub-components (e.g., dunes, supratidal beach, inter-tidal zone, and sub-tidal zone), and these sub-components tend to operate over different time scales (Castelle et al., 2017b).

A quantitative understanding of littoral cells and sediment budgets is a fundamental element of coastal sediment studies (Bowen and Inman, 1966; Caldwell, 1966; Komar, 1998; Rosati, 2005). Littoral cell (self-contained or semi-contained; refer to Fig. 1) and sediment budget concepts were introduced in the 1960s through several regional studies based upon coastal geology (rocky headlands) and estimates of longshore sand transport along specified sources and sinks (Bowen and Inman, 1966; Caldwell, 1966; Inman and Frautschy, 1966). Littoral cells are essentially defined as self-contained coastal units over a period of time, usually separated by prominent features (often headlands or jetties) that impede transfer of sediment (Kinsela et al., 2017). These cell boundaries delineate the spatial area within which the budget of sediment is known, providing the framework for the quantification of coastal erosion and accretion (CIRIA, 1996). Whether a littoral cell can be considered contained (Fig. 1-left panel) or semi-contained (Fig. 1-middle and right panels) depends on the timescale of consideration. Often, a compartment or coastal cell may appear closed, but over longer timescales during which long return period events inducing severe sediment transport are included, it may actually be open or semi-contained. Therefore, primary sediment compartments (self-contained/closed) are those that capture the limit in the sediment pathway within a large sediment-sharing area for long timescales (10^1–10^2 years);

while sub-cells are usually finer in scale, identify semi-contained/open systems at timescales > 10^1 years and can appear closed in the short-term (< 10^1 years) (Rosati, 2005; Kinsela et al., 2017; Thom et al., 2018).

Highly embayed beaches are often considered closed cells (Fig. 1-left panel) with the prominent headlands acting as barriers to littoral drift, such that sediment transport into and/or out of adjacent cells is insignificant. Nevertheless, recent studies show that significant sediment transport offshore and/or beyond these barriers exists under particular conditions, inducing headland bypassing (Short, 1985; Short and Masselink, 1999; Short, 2010; Cudaback et al., 2005; Loureiro et al., 2012; George et al., 2015; Vieira da Silva et al., 2017; McCarroll et al., 2018). Short (1985) suggested that major storm wave events are one of the key drivers of headland-attached bar bypassing, allowing sand to be transported to the morphological depth of closure *(DoC)* and beyond the headland position. Additionally, recent studies of mega-rips and beach response to extreme storm events also reveal important cross-embayment exchanges across the shoreface to deeper water (Short, 2010; Loureiro et al., 2012; McCarroll et al., 2016) and between adjacent beaches (Cudaback et al., 2005; Vieira da Silva et al., 2017). Furthermore, new research also emphasizes the influence of the strong tidal currents registered around headlands in facilitating bypassing at macrotidal environments (McCarroll et al., 2018; King et al., 2019; Valiente et al., 2019). All these studies demonstrate that under certain conditions of wave-tidal current interaction, important sediment transport paths occur at depths that well exceed the depth of the base of headlands, challenging the notion of embayments as closed coastal cells and highlighting limitations to the littoral cell and the depth of closure, critical concepts for long-term coastal evolution studies (e.g., application of the Bruun rule) and shoreline modelling (e.g., one-line models).

A total sediment budget approach to a coastal cell enables derivation of incoming and outgoing sediment fluxes from the rate of sediment volume change within the cell. A significant research gap exists in quantification of sediment budgets, in that many studies examine parts of the budget (e.g., the inter-tidal), while extremely few studies capture the entire system. This information helps with confirming the status of a closed cell and estimating the long-term coastal evolution (Wiggins et al., 2019). For a given coastal cell, the sediment budget (dQ_{net}) is expressed by the balance of volumes between sediment supply (ΣQ_{source}) and sediment losses (ΣQ_{sink}) in the compartment (Rosati, 2005; Aagaard, 2011). In both closed (Fig. 1-left panel) and balanced

systems (Fig. 1-middle panel) $dQ_{net} = 0$; however, for unbalanced systems (Fig. 1-right panel), $dQ_{net} \neq 0$ and in this case the volume of incoming sediment is not the same as the volume that exits the system. For prograding shorefaces and retrograding shorefaces, $dQ_{net} > 0$ and $dQ_{net} < 0$, respectively. Sediment sources include longshore transport of sediment into the area, cross-shore supply of sediment from offshore (beyond the cell seaward limit), anthropogenic interference (beach nourishment), in-situ production of sediment (Kinsela, 2017) and supply from autochthonous sources, such as rivers and dune and cliff erosion (Aagaard, 2011). Sediment losses from the upper shoreface can be accomplished through longshore and cross-shore processes. Sediment can leave embayments through headland bypassing, onshore aeolian transport beyond the coastal dune region (e.g., into a back-barrier lagoon) and offshore exchange from the upper shoreface to larger depths, i.e., beyond the depth of closure from where sediment may not be transported back onshore.

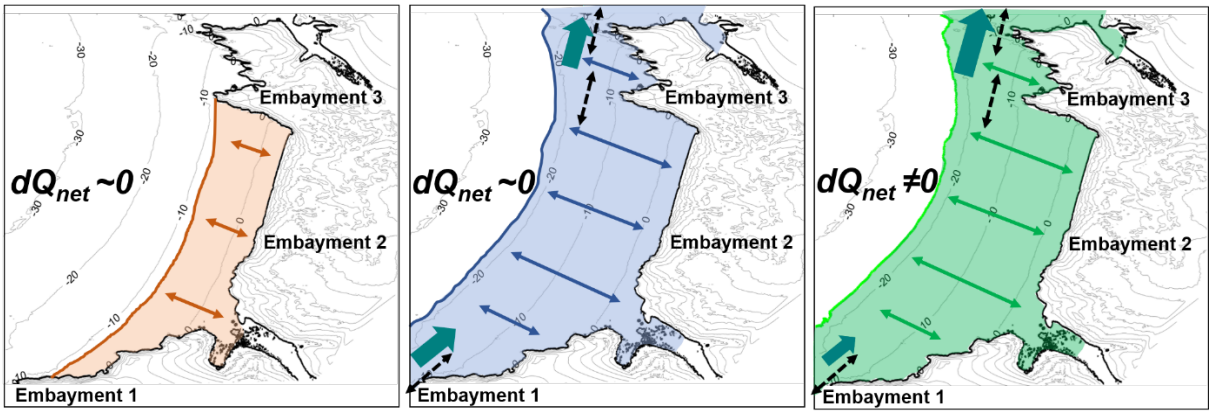

Fig. 1. Plan view of beach-inner shelf dynamics for a closed cell (left panel), a balanced open system (middle panel) and a non-balanced open system (right panel) using an idealized high-energy, cross-shore dominated and embayed coastal cell section.

Most of current coastal research based on observations lack rigorous uncertainty calculation, potentially identifying measurement artefacts as real morphological changes and consequently, misrepresenting sediment fluxes. For a robust quantification of cross-shore and longshore sediment fluxes within coastal cells, is important to distinguish real changes from noise (Lane et al., 1994; Milne and Sear, 1997; Lane, 1998; Brasington et al., 2000; Lane et al., 2003; Wheaton et al., 2010; Wiggins et al., 2019; Guisado-Pintado and Jackson, 2019). Sandy coastlines commonly exhibit vertical morphological fluctuations of similar magnitude to the uncertainty

associated with the measurement. In order to account for this uncertainty, but retain information on real morphological change, effective spatially-variable uncertainty computation techniques are required (Brasington et al., 2003; Lane et al., 2003, Wheaton et al., 2010).

In this study, we apply a total sediment budget approach based on field observations and spatially-variable uncertainty analysis. We evaluate the inter-annual dynamics of Perranporth beach, a sandy, exposed and embayed coastal system located on the north coast of SW England, over multi-annual time scales. Recent model-based studies investigated the potential for headland bypassing and offshore shoreface limits for significant sediment transport across Perranporth (McCarroll et al., 2018; Valiente et al., 2019). These indicated that the sub-tidal zone is potentially as dynamic as the rest of the beach system, and that, despite the cross-shore dominated nature of this type of embayment, alongshore processes and sediment fluxes may play an important role in the sediment balance of the system. Hence, we examine: (1) inter-annual morphological evolution of the inner embayment, including cross-shore and longshore sediment exchanges between sub-systems; (2) multi-annual full embayment morphological response to the 2013/14 winter, which represents the most energetic period along most of the European Atlantic coast since at least 1948 (Masselink et al., 2016b), using a total sediment budget approach,; (3) relationship between wave forcing and embayment response; and (4) the nature of Perranporth's coastal cell (closed or open).

A description of the study area together with the methodology applied to estimate the total sediment budget is presented in Section 2. A comprehensive analysis of quasi-full embayment beach morphology (inter-annual records of dune, inter-tidal and sub-tidal regions) is presented in Section 3. This analysis is extended spatially (for multi-annual epochs) to the full embayment (coastal cell) by including observations offshore (>-40 m Ordnance Data Newlyn, ODN) and beyond the bounding headlands for the years 2011, 2016, 2017 and 2018 in Section 4. Links between wave forcing and embayment morphological change are presented in Section 5. Section 6 presents discussion with a conceptual sediment budget model. Finally, conclusions are presented in Section 7.

2. Study area and methodology

2.1. Perranporth and Penhale Sands beach

Perran and Penhale Sands beach (hereafter noted as Perranporth beach) is a sandy, exposed, dissipative and macrotidal embayment located on the north coast of Cornwall, SW England (Fig. 2a). The configuration of the beach is typical of this coastline (Burvingt et al., 2018), which is characterized by sandy beaches embayed by sharp headlands (Fig. 2b). The site represents a 3.5-km long wide sandy beach facing 290° at the south and 280° at the north, backed by an extensive and high dune system both in the north (Fig. 2c, 60 m ODN) and south (Fig. 2d, 20 m ODN), divided by a small headland (Cotty's Point). The embayment is delineated by Ligger Point (northern end) and Droskyn Point (southern end), comprised of metamorphic rocks with 40-m high cliffs dropping near vertically (at their most offshore extent) to 2–7 m depth ODN at the south and to 5–7 m depth ODN at the north. The southern hindshore dune system is the center of numerous anthropogenic interventions that affect the natural morphologic response of that area of the beach, in contrast to the northern dunes where natural processes dominate. The beach presents a relatively featureless upper inter-tidal zone, a three-dimensional lower inter-tidal region (around MLWS), mostly characterized by inner low-tide bar/rip systems (Masselink and Short, 1993; Scott et al, 2011), and a sub-tidal outer bar oscillating between 5 to 7 m depth ODN. The shoreface is characterized by a low-gradient (mean bed slope of 0.018) with the limit of detectable morphological change or morphological depth of closure (*DoC*) at -14.5 m located 750–950 m from the mean sea level (MSL; approximately 0.3 m ODN) and a c. 500-m wide inter-tidal region. Perranporth beach is composed of medium sand with a median grain size (D_{50}) of 0.33–0.40 mm for the supra- and inter-tidal area (Prodger et al., 2017). The D_{50} attains a relatively constant value of 0.30 mm for the sub-tidal area with gravel patches (D_{50} = 2–3 mm) appearing around 26 m depth ODN (Valiente et al., 2019).

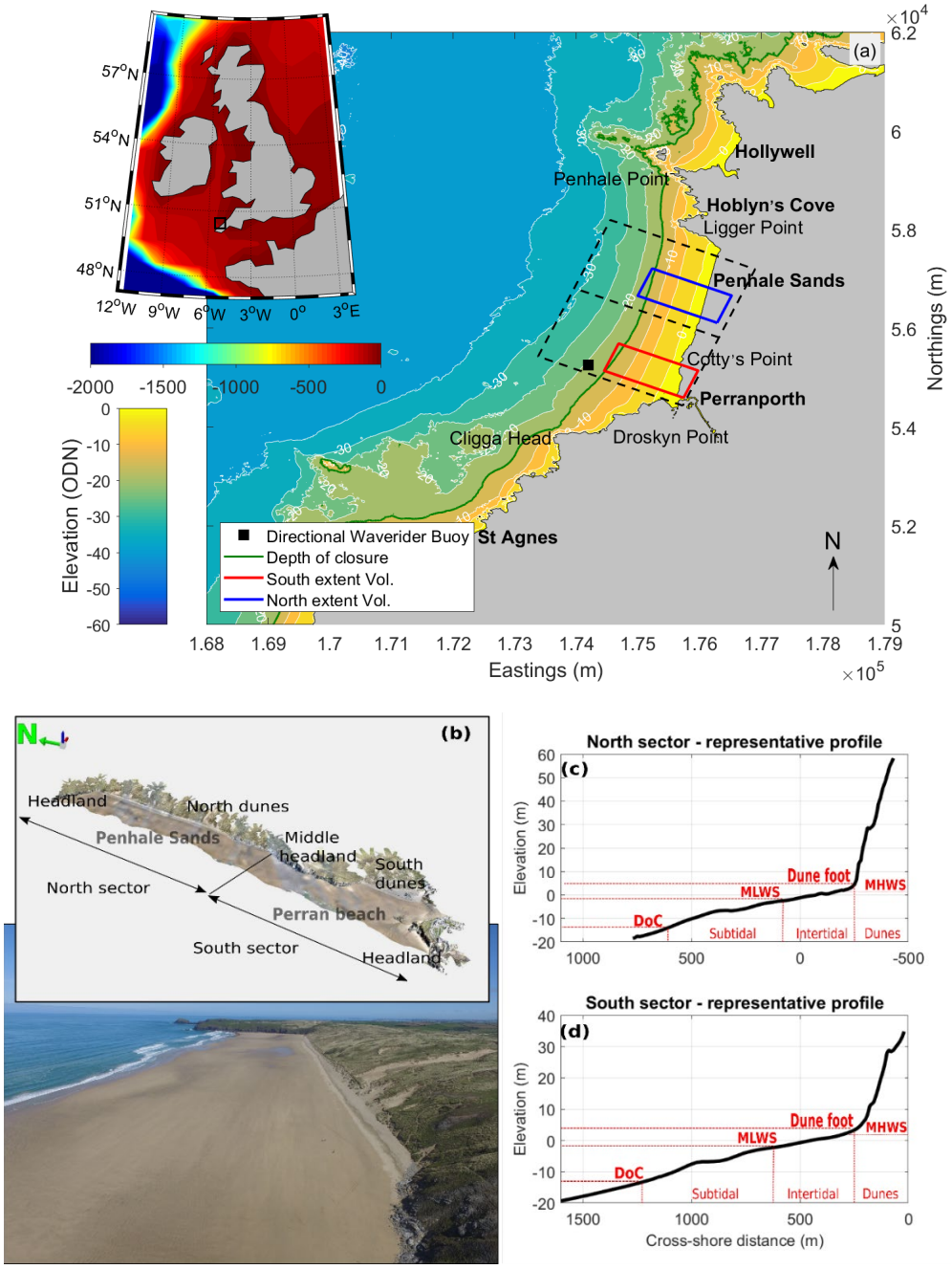

Fig. 2. (a) Location map of Perranporth beach, SW England, physical context and regions used for quasi and full embayment volume time series calculation (red and blue boxes, and black dashed region, respectively). (b) Embayment 3D-view with extension of north and south sectors and aerial photograph of Penhale Sands taken to the north showing north dune system. Bottom right-hand panels show a representation of a vertical profile from the frontal dune system to the inner-shelf for the north (c) and south (d) beach sectors, including the considered sub-systems (sub-tidal, inter-tidal and dunes).

Perranporth is exposed to regular North Atlantic swell with an annual average significant wave height (H_s) of 1.6 m and peak period (T_p) of 10.2 s, and storm events with a 1% exceedance wave height and associated peak wave period of 4.6 m and 16.7 s, respectively (Fig. 3e). Incoming wave energy displays strong seasonal modulation (Fig. 3a-b) with monthly average H_s ranging from 1.2 m (June) to 2.3 m (January) over the period 2007–2018. Wave approach is typically from the W (0.5 probability) and WNW (0.4 probability), with the larger winter waves also slightly more northerly in direction (WNW: $H_{s,50\%} = 1.6$ m; W: $H_{s,50\%} = 1.3$ m; WNW: $H_{s,1\%} = 5.2$ m; W: $H_{s,1\%} = 4$ m) (Fig. 3d). Therefore, winters are associated with peaks in southerly-directed (negative) alongshore wave power (P_y) (Fig. 3f). The tidal regime is semi-diurnal and macrotidal with a mean spring and neap tidal range of 6.3 m and 2.7 m, respectively (Masselink et al., 2014; Scott et al., 2016). Tidal currents with values of c. 0.7 m s^{-1} are registered during spring tides near the headlands (Valiente et al., 2019). The flood-ebb asymmetry in the current magnitude during a tidal cycle results in a northward tidal net residual current along the embayment (McCarroll et al., 2018), in particular near the northern headland. Computed bed shear stresses, reinforced by observations of sediment distribution within the embayment, suggest that wave-driven currents during extreme storm events can induce energetic sediment transport well seaward of the *DoC*, even when disregarding tidal action (Valiente et al., 2019). When also considering tidal currents during the maximum flood in a tidal cycle, the depth limit for this dynamically active shoreface increases by more than 5 m, reaching 28 m depth ODN (Valiente et al., 2019).

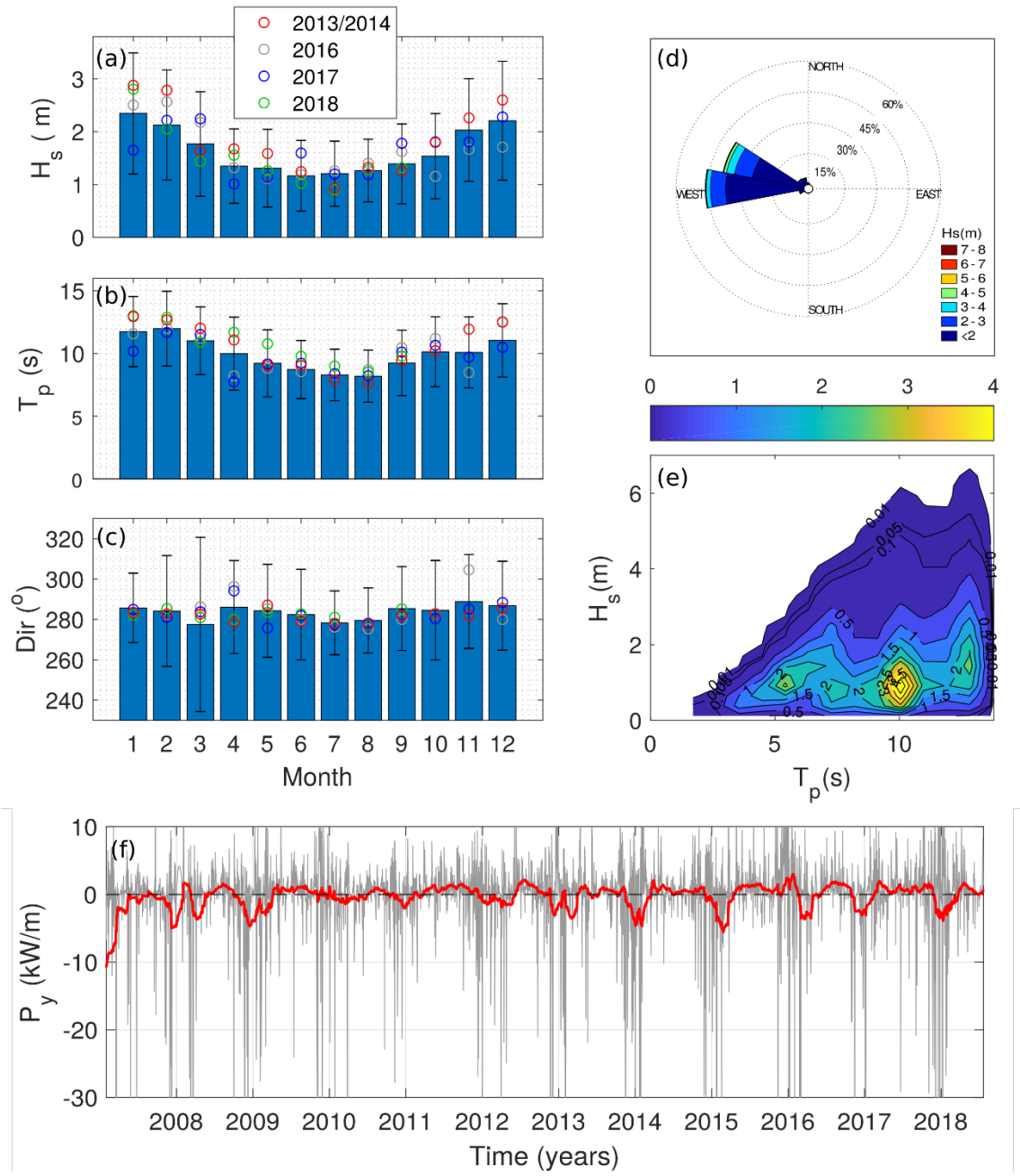

Fig. 3. Monthly statistics of: (a) significant wave height; and (b) peak wave period; and (c) wave direction, computed for the period 2007–2018. Wave statistics were derived from the Perranporth directional waverider buoy (refer to Fig. 2a for location). In all left panels, bars indicate monthly-averaged values with error bars showing the monthly standard deviation and circles indicating 2013/2014 and years 2016–2018 monthly-averaged values. (d) Directional wave rose showing distribution of H_s and (e) joint probability of H_s and T_p with percentage occurrence contours. (f) 11-year time series of alongshore wave power, P_y (1-day and 8-week running mean) for an averaged orientation of c. 285°. Southward P_y is negative.

2.2. Multimethod morphological surveys

The complete dataset used in this paper is complex as it involves various survey methods at a range of spatial and temporal extents. Fig. 4 provides an overview of the coverage of the dataset collected by the Coastal Processes Research Group (CPRG), University of Plymouth, and the Plymouth Coastal Observatory (PCO) since October 2006. The south part of the beach has been monitored for over 11 years, whereas the northern part has only been surveyed since 2016.

Monthly inter-tidal beach surveys covering the south part of the beach (red box; Fig. 2a) were conducted since October 2006. Airborne LiDAR datasets that cover the inter-tidal beach and dune system of the whole beach, obtained from PCO, are available for 2008, 2009, 2011, 2012, 2014, 2016 and 2017. The monthly inter-tidal all-terrain vehicle (ATV) based real-time kinematic Global Positioning System (RTK-GPS) surveys of the south area of the beach are complimented with quasi-quarterly single-beam echosounder bathymetric surveys (herein SBE) for the sub-tidal zone during the period 2010–2012 and 2014–2018. Only since 2016 was the survey program specifically designed to enable quantification of the total sediment budget and net sediment fluxes for Perranporth beach, and multi-method morphological surveys capturing the entire beach (black dashed box; Fig. 2a) from May 2016 were performed during spring and autumn. The sub-tidal coverage was extended (down to a depth of -40 m ODN) through conducting yearly (spring/summer) multi-beam echosounder bathymetric surveys (herein MBE). Despite great efforts to collect sub-tidal data, Perranporth is an exposed high-energy environment and areas in close proximity to headlands were too hazardous to survey due to exposed rocks and breaking waves, and hence are not covered in this analysis.

Photogrammetric data of the south and north dunes were collected using an DJI Phantom 4 quadcopter (herein unmanned aerial vehicle; UAV), covering the supratidal up to an elevation of 30 m ODN. Ground control points (GCPs) were vertically and horizontally distributed throughout the survey region at intervals of 100–250 m and were surveyed by RTK-GPS for constraining bundle adjustment during Structure-from-Motion post-processing workflow. The inter-tidal and supratidal zone was surveyed using ATV-based Trimble 5800 RTK-GPS, with line spacing of 20–25 m. The shallower sub-tidal data were collected using a Valeport Midas Surveyor single-beam echosounder with a 210 KHz transducer with a sample rate of 6 Hz mounted on an Arancia inshore rescue boat (IRB) and external Trimble 5800 RTK-GPS positioning. These

bathymetric surveys were conducted following cross-shore transects at 50-m spacing for inshore lines (< 10 m depth) and 100-m spacing for offshore lines (> 10 m depth). Yearly multi-beam echosounder bathymetric surveys were collected using a pole-mounted 400 kHz R2Sonic 2024 MBES, with motion data provided by a vessel-mounted GNSS-aided Applanix POSMV MRU and primary positioning provided by a Trimble SPS RTK-GPS system.

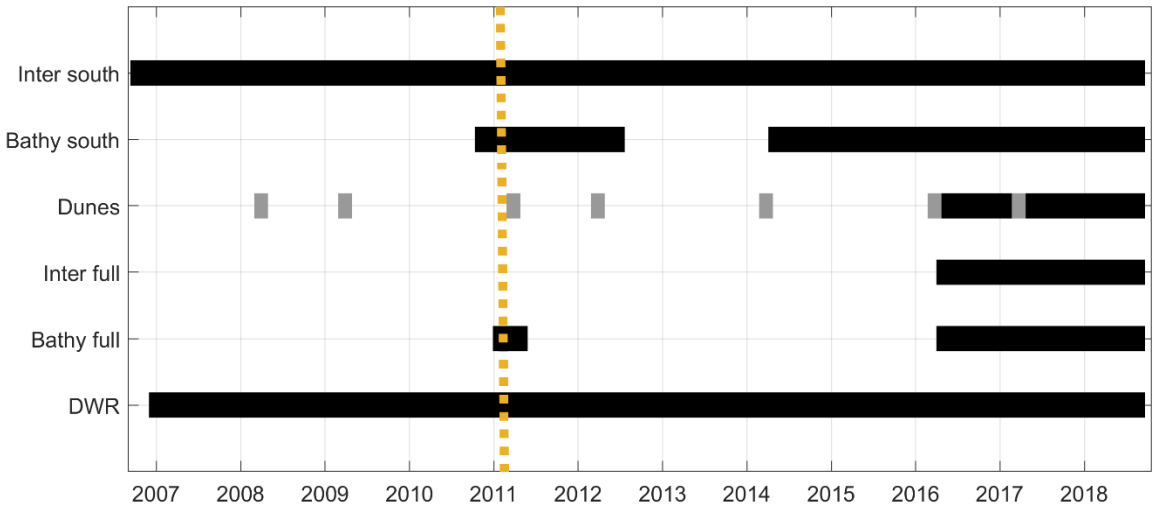

Fig. 4. Timeline of the data sources available for analysis. From top: Perranporth beach inter-tidal beach morphology (Inter south), Perranporth beach sub-tidal bathymetry (Bathy south), full embayment dune morphology from LiDAR and UAV (Dunes), full embayment inter-tidal beach morphology (Inter full), full embayment sub-tidal bathymetry (Bathy full) and directional wave rider buoy (DWR). Grey stripes show years for which LiDAR data are available. Orange dashed line represents winter 2011 reference state.

2.3. DEM creation

Three sets of 2-m gridded digital elevation models (*DEMs*) were constructed from composite datasets: (1) 27 *DEMs* covering the southern inter- and sub-tidal beach for the period 2010–2018 (red box, Fig 2a); (2) 6 seasonal *DEMs* covering the quasi full embayment (black dashed box down to *DoC*, Fig 2a) from the sub-tidal to the dunes (included), hereafter referred to as the 'inner embayment', for the period 2016–2018; and (3) 3 *DEMs* covering the entire embayment including adjacent areas beyond the bounding inner headlands (including depths > 18 m), hereafter 'full embayment', for the years 2011, 2016 and 2018 (Table 1). Topographic (RTK-GPS) and bathymetric (SBE) measurements (RTK+SBE; 27 *DEMs*) were combined using a Loess interpolation function (Plant et al., 2002), with variable smoothing scales and maximum

permissible interpolation error level of 0.15 m. Individual UAV, RTK+SBE and MBE datasets were combined for the final multimethod full embayment *DEM* construction with natural neighbor interpolation function (Sibson, 1981).

To determine the impacts of the 2013/14 winter storms on the Perranporth beach sediment budget, an additional full embayment dataset for the year 2011 was constructed by combining LiDAR and multi-beam bathymetry, corrected and referenced to ODN using the Vertical Offshore Reference Frame separation model (VORF) facilitated by the United Kingdom Hydrographic Office.

Table 1. Component gridded datasets and calculated uncertainty ($\boldsymbol{\sigma}$) included in the 3 full embayment DEMs

Name	Method	Date	Coverage	Calculated uncertainty, σ (m)
2011 DEM	LiDAR	01/2011	Dunes, supra- and inter-tidal (-2–>30 m)	0.15
	SBE	01/2011	Sub-tidal (-10–-2 m)	0.05
	MBE	2011, not specified	Sub-tidal (<-7 m)	0.27
2016 DEM	UAV	04/2016	Dunes (4–>30 m)	0.06
	RTK	04/2016	Supra- and inter-tidal (-2–4 m)	0.04
	SBE	04/2016	Sub-tidal (-18–-2 m)	0.05
	MBE	08/2016	Sub-tidal (-16–<-30 m)	0.06 – 0.3 *
2018 DEM	UAV	09/2018	Dunes (4–>30 m)	0.06
	RTK	09/2018	Supra- and inter-tidal (-2–4 m)	0.05
	SBE	09/2018	Sub-tidal (-18–-2 m)	0.05
	MBE	06/2018	Sub-tidal (-16–<-30 m)	0.06 – 0.3 *

*majority of values < 0.15 with maximum values registered around a rocky platform at the northern sector outside the embayment domain

2.4. Full embayment volume change computation

Full embayment morphological measurements were used to calculate volume change and derive net sediment fluxes following a total sediment approach and accounting for gridded uncertainty through the domains. Several approaches to quantifying the total sediment budget of a coastal cell exist (Van Rijn, 1997; Cowell et al., 2003; Aagaard, 2011; Van Rijn, 2011); however, none of these account for the associated uncertainty (σ_{DEM}) in the volume computation. Here, we follow the methodology proposed by Wheaton et al. (2010) applied to rivers and later used by

Wiggins et al. (2019) for application to gravel beach environments. This methodology consists of three main steps: (1) computing the surface uncertainty associated with the digital elevation model (*DEM*); (2) quantifying the *DEM* of difference ($DoD = Z_{DEM_1} - Z_{DEM_2}$) and the propagated uncertainty or minimum level of detection, $minLoD = \sqrt{(\sigma^2_{DEM_1} + \sigma^2_{DEM_2})}$ for a defined confidence level (95% in this instance); and (3) only considering significant bed-level changes by disregarding elevation changes that are less than the *minLoD* value (herein *LoD*).

Estimates of net morphological change are fundamentally controlled by *DEM* quality, itself largely inherited from the quality of the survey data (Wise, 1998; Wechsler, 2003; Wechsler and Kroll, 2006; Wheaton et al., 2010). We quantify the quality of each *DEM* using a spatially variable uncertainty which is the result of the combination of the spatially uniform (UAV, inter-tidal RTK-GPS and sub-tidal SBE) and spatially variable (MBE) surfaces presented in Table 1. Associated uniform uncertainty of the UAV survey technique was extracted from Wiggins et al. (2019), who applies a UAV model comparison to an absolute reference control surface on a gravel beach. Due to the lack of a control surface to compare to RTK and SBE techniques, uncertainty surfaces for these methods were calculated computing instrument and interpolation uncertainties individually and then added using a quadratic sum (Taylor, 1997). RTK instrument error (2σ for 95% confidence level; Brasington et al., 2000) was estimated using the vertical deviation in repeated control points over 3 years (~35 observations); while SBE instrument error was extracted from the standard deviation of the actual SBE measured points with respect to overlapped RTK-GPS topographic points along a testing control line of 1000 m (facilitated by large tidal range). For both methods, standard deviation values between the raw input data and the resulting interpolated grids within a control region of 50x50 m were used as interpolation error. MBE spatially variable residual uncertainty surface was based on total propagated uncertainty (TPU) values for each individual sounding (generated through QPS QINSy/Qimera hydrographic software) which were then gridded using the Combined Uncertainty and Bathymetric Estimator (CUBE) algorithm (Calder and Mayer, 2003; Calder and Wells, 2007; Schimel et al., 2015). The vertical accuracy of the only externally sourced MBE dataset (for 2011) was based on the known survey specification (International Hydrographic Organization Order 1a). This was relatively large (σ = 0.27 m), but provided the only opportunity to obtain a full embayment survey prior to 2013.

Finally, the total volume difference or total sediment budget and associated uncertainty were quantified using the non-discarded *DoD* values, $|Z_{DEM_1} - Z_{DEM_2}| \geq minLoD$ for a 95% confidence level. Sediment volumes (in m^3 per meter width) were computed for different sections of the beach profile: dune (> 30 to 5 m ODN), supra- and inter-tidal (5 to -2 m ODN) and present sub-tidal (beyond -2 m ODN). To avoid errors in the dune volume computation, the vegetated areas not comprising part of the active beach system were discarded. The beach was also divided into northern and southern sections (divided black dashed box, Fig 2a), allowing a full embayment investigation of embayment-scale alongshore variability in volumes. It is noted that alongshore variability refers to volumetric differences between south and north, and not small scale alongshore variability associated with bar/ rip morphology.

3. Quasi full embayment beach response and evolution (volume time series)

Fig. 5 shows beach volumetric time series for each of the sub-systems considered (dunes, inter-tidal and sub-tidal) for the north and south sectors of the beach (red and blue boxes, Fig. 2a). Sediment volumes are plotted relative to the reference state, January 2011, as a topographic and bathymetric survey is available for that time for both north and south sectors of the beach. The beach/dune morphology is significantly different for the two sectors: the inter-tidal beach in the north is narrower than in the south (refer to Fig. 2c,d) and, the front of the northern dune system is characterised by a high and steep ramp, whereas the southern dune system is fronted by a developing fore dune.

The two regions also show markedly contrasting behavior in terms of dune volumetric change. Over the monitoring period, the southern dune system has progressively accreted 5,550 m^3 (30 m^3 m^{-1}), representing 800 m^3 $year^{-1}$ (4 m^3 m^{-1} $year^{-1}$). The northern dune system, on the other hand, has remained relatively stable over the period 2008–2013, but during the 2013/14 winter, 80,000 m^3 was lost (50 m^3 m^{-1}, accompanied by total retreat of the dune foot of c. 15 m) with no significant post-event recovery. The dune ramp is still located 7 m landward of the pre-2013/14 dune face 4 years later, without a developing fore dune. The dune volume time series also shows a modest seasonal modulation (amplitude c. 15 m^3 m^{-1}), largely due to the advance/retreat of the dune foot during the summer/winter cycle.

Inter-tidal volumetric changes are shown in Fig. 5c for the south (11-year time series) and for the north (2.5-year time series) sectors. The southern inter-tidal time series displays both

seasonal (amplitude c. 50 m^3 m^{-1}, refer to Fig. 5c) and multi-annual event response signals (amplitude c. 200 m^3 m^{-1}, refer to Fig. 5c). Specifically, the southern time series started (October 2006) in a fully accreted state (+50 m^3 m^{-1} with respect the reference state), then experienced significant erosion (c. 180 m^3 m^{-1}) during the 2006/7 winter ($H_{s,50\%}$ = 2.4 m), followed by a 3–5 year recovery (up to October 2010) to a stable fully accreted state. The intense storms during the 2013/14 winter (red circles Fig. 3a, $H_{s,50\%}$ = 2.7 m) resulted in sediment losses in excess of 200 m^3 m^{-1} in the south. Following the 2013/14 winter, an increase in alongshore volume standard deviation (Fig. 5c) was observed during the 2014–2017 recovery period. According to Scott et al. (2016), this is associated with the development of large-scale three-dimensional sandbar morphology in the lower inter-tidal region during beach recovery phases (see also Poate et al., 2014). Post 2013/14 winter, southern and northern beach volumes experienced a multi-annual recovery phase within which significant seasonal variability was observed (for example, an energetic 2015/16 winter (H_s = 2.6 m), resulted in 140 m^3 m^{-1} loss in the south). By autumn 2018 (4.5 years after 2013/14 storms), the south beach had recovered by 88%.

Examining the 10-year time series of beach sediment volume (Fig. 5), a surprising observation is that the inter- and sub-tidal volumes do not exhibit the inverse correlation expected for a cross-shore dominated beach, suggesting that alongshore sediment fluxes are significant. Indeed, there appears to be a positive correlation between southern inter-tidal volume and sub-tidal volume, with a time lag of approximately 1-year (e.g., compare the 2013-2014 decrease in inter-tidal volume with the 2014-2015 decrease in sub-tidal volume). The imbalance in total volume for the south sector was previously alluded to by Scott et al. (2016), who examined the 2013/14 storm response for a 250-m southern sector of Perranporth and found that the inter-tidal zone lost >200 m^3 m^{-1}, while the sub-tidal zone only gained 110 m^3 m^{-1}. The monthly time series of sediment volume for the southern region (Fig. 5c-e) clearly demonstrates that the inter- and sub-tidal volumes do not balance. For example: (1) from October 2010 to July 2012, the sub-tidal gained c. 200 m^3 m^{-1} of sediment, whereas the inter-tidal sediment volume remained relative constant (ignoring seasonal fluctuations); (2) from May 2014 to February 2015, the sub-tidal lost c. 300 m^3 m^{-1} of sediment, whereas the inter-tidal gained c. 100 m^3 m^{-1} of sediment; and (3) from March 2017 to May 2018, the sub-tidal gained c. 200 m^3 m^{-1} of sediment, whereas the inter-tidal sediment volume lost c. 30 m^3 m^{-1}. These observations for the southern region strongly point to the presence of significant longshore exchange of sediment, either within the embayment or

beyond the southern extend of the region, and/or offshore sediment transport beyond the detectable *DOC*.

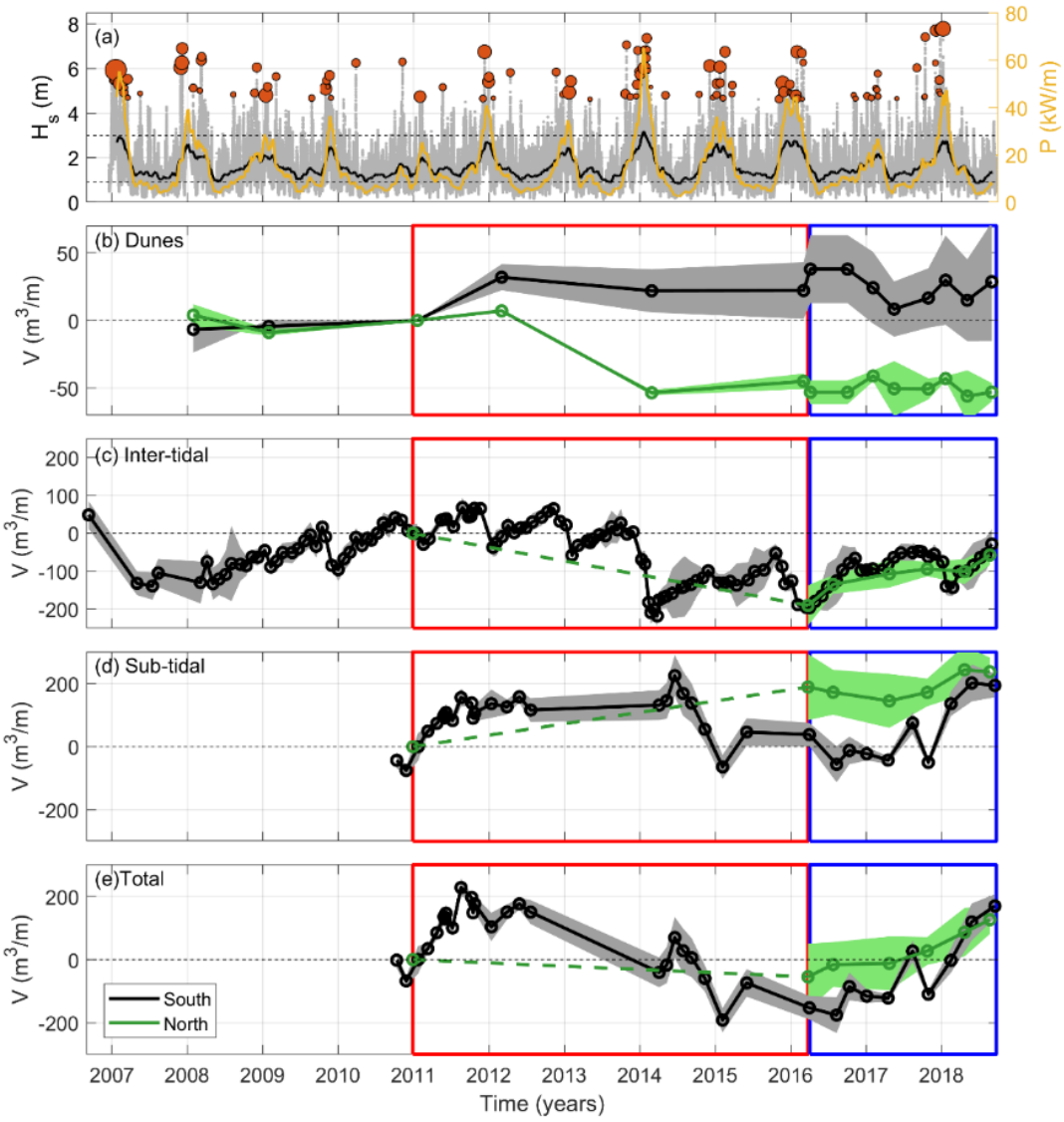

Fig. 5. South (black) and north (green) Perranporth beach response and evolution. (a) 11-year time series of significant wave height measured at Perranporth wave buoy (30-min and 8-week running mean), wave power *P* (Herbich, 2000) and storm events (orange bubbles, $H_s > H_{s,99\%}$, minimum of 6 hours duration and a meteorological independence criterion of 24 h between peaks). The size of the bubbles is proportional to storm duration based on $H_{s,95\%}$ cut-off. Dune (b), inter-tidal (c) and sub-tidal (d) sediment volume (m^3 m^{-1} alongshore-averaged) and associated alongshore standard deviation (bounded area). (e) Total beach sediment volume (m^3 m^{-1} alongshore-averaged, from dune foot to -14.5 m ODN) and associated alongshore standard deviation (bounded area). Dune volume refers to the area above the dune foot (z = 5), inter-tidal volume corresponds with the area from the dune foot to z = -2 m ODN and sub-tidal from z = -2 m to -14.5 m ODN. Red (storm) and blue (recovery) squares represent the considered epochs in Section 4.

When the more discontinuous sediment volume time series for the northern region is also considered, an alongshore quasi-coherent response is observed. For the period 2016–2018, the inter-tidal accretion for the northern and southern sectors of the beach are very similar (130–160 $m^3\ m^{-1}$). Over that same period, the sub-tidal region also accretes, but the accretion in the northern region (c. 50 $m^3\ m^{-1}$) is significantly smaller than in the southern region (c. 160 $m^3\ m^{-1}$). Importantly, the total sediment volume for both the southern and northern region increase during this period by a very substantive amount (200–300 $m^3\ m^{-1}$). This strongly suggests that the inner embayment is not 'closed' (cf. Fig. 1) and that sediment may be transported alongshore, potentially around the terminating headlands, and/or offshore beyond the detectable *DoC*, and/or onshore into the vegetated dune area. To robustly examine the sediment fluxes within and beyond the inner embayment and quantify the sediment fluxes between the different sub-systems, it is necessary to take a total sediment budget approach, expanding both the alongshore and cross-shore spatial coverage, and accounting for propagated volumetric uncertainty. The following section examines the two epochs where full embayment coverage is available.

4. Full embayment total sediment budget

In this section we will present the full embayment analysis for two epochs, representing extreme storm response (Fig. 6) and post-storm recovery (Fig. 7). The results for both epochs are then summarized in Fig. 8 and Table 2. It is noted that in the figures the sediment volume changes are presented in units of m^3 per unit meter beach width, whereas in the table the total volume changes in m^3 are listed.

4.1. Storm response

Full embayment *DEMs* for the years 2011 and 2016 were used to further investigate cross-shore sub-compartment sediment fluxes and along-coast sediment exchange, within and beyond the inner embayment, surrounding the high energy 2013/14 winter period. The lack of a full embayment morphological dataset bracketing the 2013/14 winter forced us to extend the period from 2011 to 2016. This is considered acceptable in terms of dune and inter-tidal volumetric changes as beach volumes in 2011 were similar to that of 2013, and the volumes for 2014 were similar to that of 2016 (refer to Fig. 5b-c). We also acknowledge that total embayment response over this epoch disregards both the dramatic accretion in the southern sub-tidal region during 2011

(>100 m^3 m^{-1}; Fig. 5d) and the significant inter-tidal erosion during winter 2015/16 (-150 m^3 m^{-1}; Fig. 5c), meaning that embayment response to the 2013/14 events could potentially have been different than shown.

The difference *DEM*, offshore acoustic backscatter and along-coast variation in sub-compartment sediment volumes are presented in Fig. 6. Light colors in the acoustic backscatter image indicate presence of medium sand, interrupted by gravel patches (dark colors) around 26 m depth ODN. It is emphasized that for the sediment volume considerations, only those bed-level changes that exceed the *LoD* (95% uncertainty level) are considered, and a large portion of the deeper sub-tidal is therefore discarded as the measured changes are considered insignificant (uncoloured parts of Fig. 6). The salient features of the storm response are: (1) extensive erosion of the front of the dunes in the north part of the beachfront (c. 50 m^3 m^{-1}); (2) erosion across the entire supra- and inter-tidal beach (c. 190 m^3 m^{-1}); (3) erosion in the shallow sub-tidal zone up to 6–7 m depth ODN; and (4) accretion in the deeper sub-tidal zone up to and even beyond the *DoC* at 14.5 m depth ODN (0–250 m^3 m^{-1}).

Integrating the positive and negative sediment volumetric changes across the entire beach to the *DoC* (Fig. 8-top panel) robustly demonstrates that the full embayment sediment budget is not balanced: there is a net loss of 280,000 m^3 and an associated uncertainty of 206,000 m^3 (Table 2). There is also a considerable longshore variability in the morphological response and this is better demonstrated when the sediment volumes are summed across the different sub-compartments for the different sections of the beach (north versus south, Fig. 8 and Table 2). Over the period 2011–2016, the northern and southern sectors of the beach lost 50,000 m^3 and 230,000 m^3 of sediment, respectively. These values represent losses per unit meter beach of 36 m^3 m^{-1} in the north and 164 m^3 m^{-1} in the south (although northern volume change is within uncertainty bounds therefore not significant at 95% level).

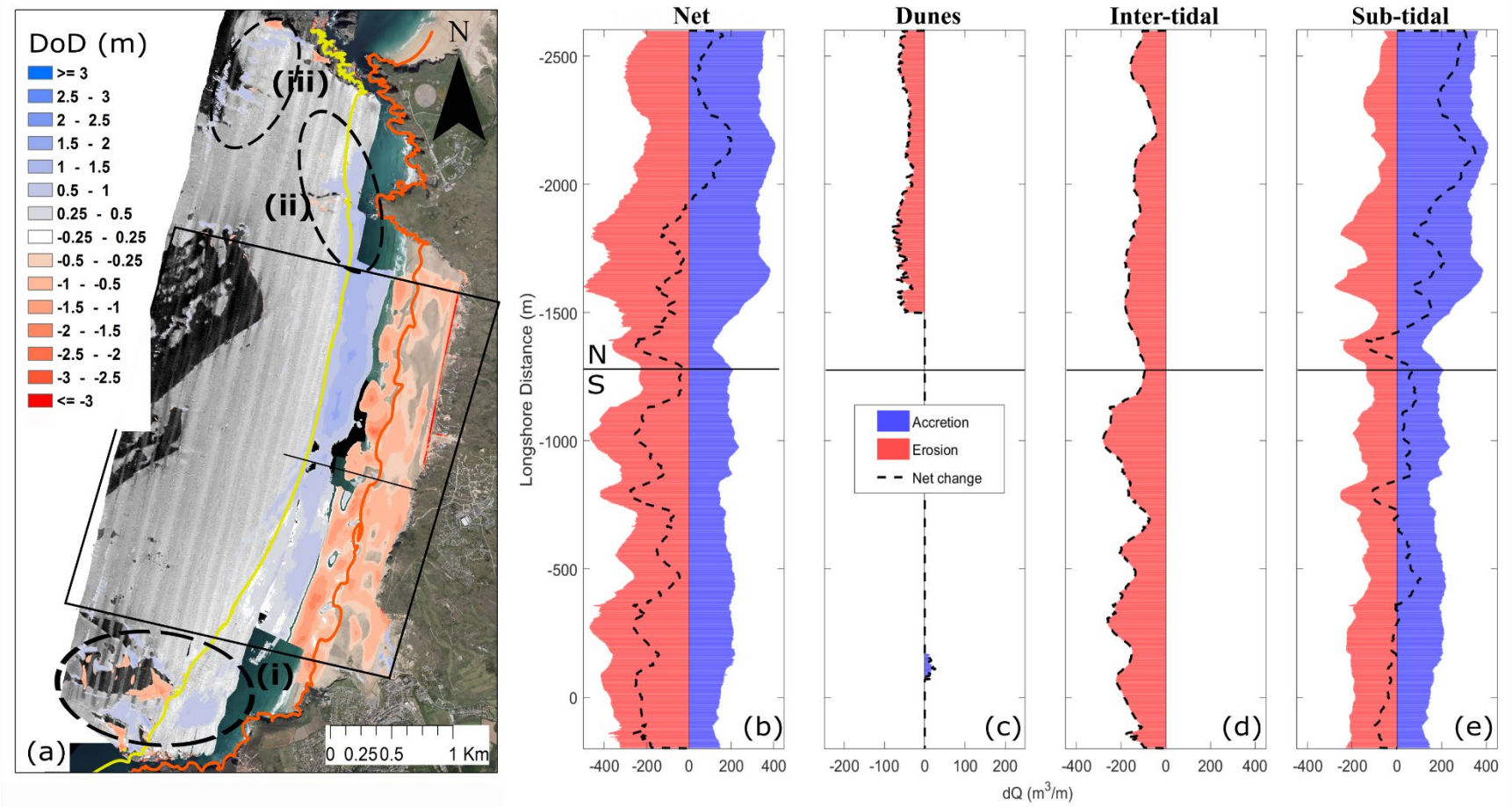

Fig. 6. Storm response total sediment budget. Left panel: full embayment *DoD* from 2011 to 2016. Areas where morphological change is not significant ($\left|Z_{DEM_1} - Z_{DEM_2}\right| \geq minLoD_{95\%}$) are uncoloured. Orange and yellow contours represent the inter-tidal to sub-tidal limit (-2 m, ODN) and *DoC* (-14.5 m, ODN) respectively. Right panels: cross-shore and alongshore variability of sediment fluxes for the complete cross-shore profile and the different sub-systems for the domain comprised inside the black box.

Morphological changes beyond the *DoC* and the lateral extent of box (Fig. 6a), referred to as 'outer embayment', are analysed to investigate possible sediment pathways in/out the inner embayment. The region beyond the *DoC* (within the box, Fig. 6) showed a small, but significant gain of 76,000 m^3 (with uncertainty of 50,000 m^3), and regions beyond the lateral extents of the box (represented by ellipses in Fig. 6) indicated significant gains with a combined total of 180,000 m^3 (uncertainty of 120,000 m^3). The gains beyond the lateral extents of the box are related to three regions. Two are offshore regions at the full embayment extents: one in the south of the study area in proximity to the Cligga Head, the southern embayment boundary (Fig. 6a-i), located between 14.5 and 26 m depth ODN; and the second located near Penhale Point, the northern of embayment boundary (Fig. 6a-iii), where only accretion occurred. The third region, alongshore to the north of Ligger Point, experienced significant sediment gains offshore of the headland (accretion of 0.6–0.8 m) and in the region of Hoblyn's Cove (Fig. 6a-ii) providing a possible sink for sediment lost from the inner embayment. While the total sediment budget cannot be entirely resolved in these regions due to lack of data in the nearshore (data collection too hazardous), these observations suggest major morphological losses from within the inner embayment are linked primarily to inner headland bypassing mechanisms, rather than cross-shore exchange beyond the depth of closure within the inner embayment, suggesting that significant sediment transport occurs seaward of the base of the inner headlands (Ligger and Droskyn) and beyond the morphological depth of closure at the embayment extremities.

4.2. Multi-annual beach recovery

Full embayment *DEMs* for the years 2016 and 2018 were compared to further investigate multi-annual sediment fluxes during a recovery period within and beyond the central embayment (black box, Fig. 7a). Fig. 7a shows the *DoD* for the entire epoch 2016–2018. The 2.5 years of recovery show a system that is not balanced, but has a net gain of 670,000 m^3 with an associated uncertainty of 180,000 m^3 (Table 2). Similar to the storm period, sediment inflows and outflows occur primarily between the inter- and the sub-tidal sub-systems (Fig. 8). Overall, both inter- and sub-tidal sub-systems accreted, mostly in the south, and although the dunes continued losing sediment (11,000 m^3 erosion, uncertainty of 3,000 m^3), the embayment is fully recovered from the 2013/14 winter in terms of net sediment budget (Fig. 7).

The key morphological responses over the recovery period are: (1) limited dune recovery; (2) accretion across the entire inter-tidal beach (143 m^3 m^{-1}); (3) accretion in the shallow sub-tidal down to 6 m depth ODN; and (4) significant longshore variability in the deeper sub-tidal area down to (and beyond in certain sectors) the *DoC*. The latter observation manifests in an alongshore gradient in the sub-tidal accretionary rates from 50 m^3 m^{-1} in the north to 150 m^3 m^{-1} in the south. Hence, morphological changes during the 2.5-year period of recovery ($dQ_{out} << dQ_{in}$) show an accretion of the supra- and inter-tidal sectors, not matched by sub-tidal erosion.

The influx of sediment into the inner embayment leading to recovery is interpreted as a combined response of entrainment of sediment sourced from greater depths (beyond the morphological *DoC*) and/or outside the headlands that delineate the system (from lateral sub-embayments). This supposition is supported by the recorded loss of sediment (-23,000 m^3) from within the *DoC* in Hoblyn's Cove sub-embayment (shown in available data to the north of the inner embayment, Fig. 7a-ii), where the bed was lowered 0.3–0.6 m. While a small proportion of net losses, it provides an indication of possible source regions and transport mechanisms. Additionally, the alongshore continuity of the *DoC* contour located beyond the headland bases (620 m in the south and 170 m in the north), in combination with the morphological change detected beyond the embayment limits, strongly suggests that Perranporth beach is part of an extended coastal cell, not just during high energy events. Despite the large uncertainty associated with offshore areas, localised accumulation patterns similar to those shown in the 2011/16 *DoD*, and located between 14.5 and 26 m depth ODN in the south and far north of the survey area, are also present during the accretionary period (dashed ellipsoids, Fig. 7a-i,iii). The possible processes and forcing mechanisms leading to embayment recovery are further examined in Sections 5 and 6.

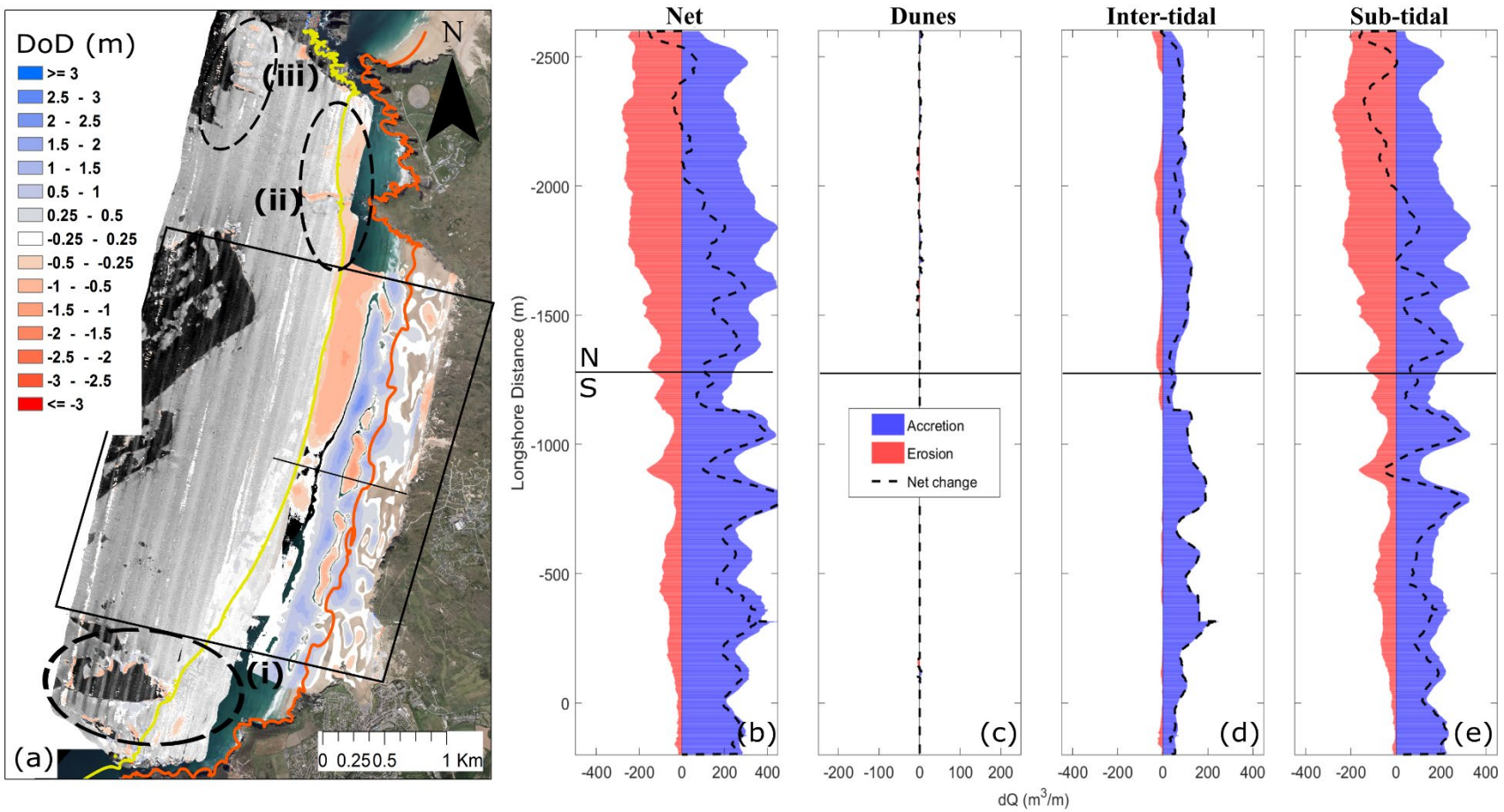

Fig. 7. Multi-annual recovery total sediment budget. Left panel: full embayment *DoD* from 2016 to 2018. Areas where morphological change is not significant ($\left|Z_{DEM_1} - Z_{DEM_2}\right| \geq minLoD_{95\%}$) are uncoloured. Orange and yellow contours represent the inter-tidal to sub-tidal limit (-2 m, ODN) and *DoC* (-14.5 m, ODN) respectively. Right panels: cross-shore and alongshore variability of sediment fluxes for the complete cross-shore profile and the different sub-systems for the domain comprised inside the black box.

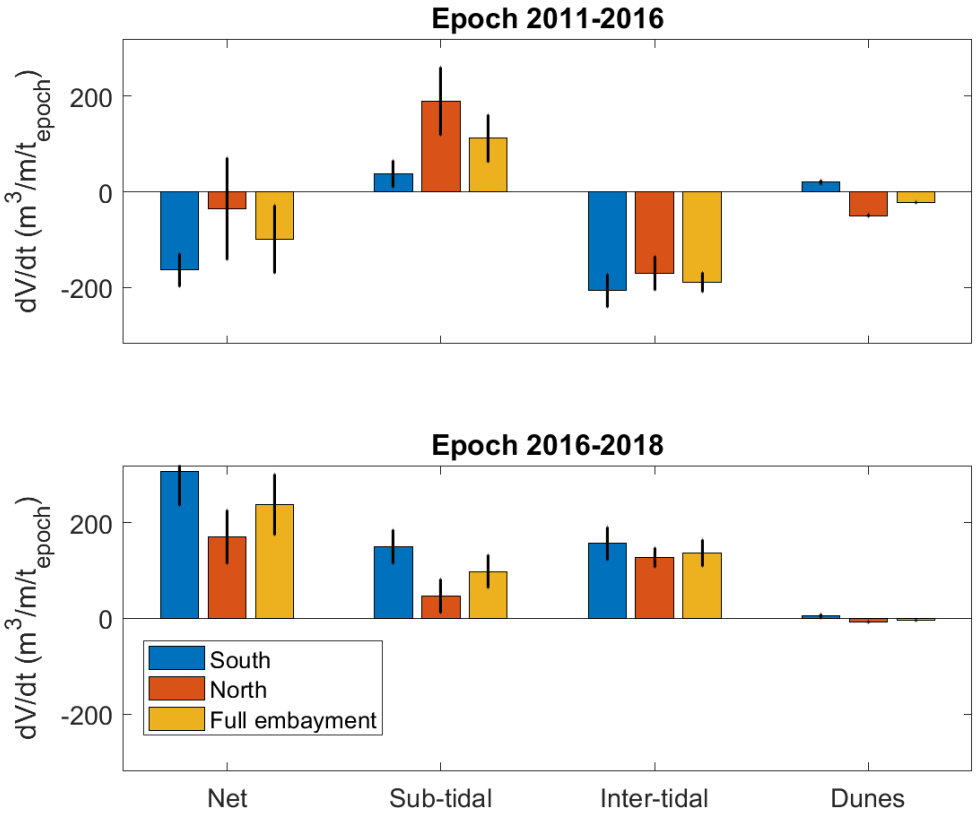

Fig. 8. Averaged sub-tidal, inter-tidal and dune volume per beach width (m^3 m^{-1} alongshore) and associated uncertainty (error bars) for epochs 2011–2016 and 2016–2018. Alongshore-averaged volumes are presented for north (1400-m alongshore) and south (1400-m alongshore) domains, except for the case of south dunes (100-m alongshore). Dune volume correspond with regions > 5 m ODN, inter-tidal volume from 5 m to -2 m ODN and sub-tidal volume corresponds with the regions from -2 m to -14.5 m ODN.

Table 2. Net volumetric changes (m^3) and associated uncertainty in sub-tidal, inter-tidal and dune sub-systems for epochs 2011–2016 and 2016–2018. Volumes are presented for north and south domains. Inter-tidal volume corresponds with the area from the dune foot (z=5 m) to -2 m and sub-tidal volume corresponds with the area from -14.5 to -2 m, inter- and supratidal from -2 to the dune foot (z=5 m) and dunes beyond z=5 m

EPOCH	*Sector*	ΔV_{net} (m^3)	$\Delta V_{sub\text{-}tidal}$ (m^3)	$\Delta V_{inter\text{-}tidal}$ (m^3)	ΔV_{dunes} (m^3)
2011-2016	*Full**		$-2.8\times10^5\pm2\times10^5$		
	*Outer***		$2.7\times10^5\pm2.4\times10^5$		
	North	$-5\times10^4\pm1.5\times10^5$	$2.6\times10^5\pm1\times10^5$	$-2.4\times10^5\pm5\times10^4$	$-7\times10^4\pm3\times10^3$
	South	$-2.3\times10^5\pm5\times10^4$	$5.3\times10^4\pm6\times10^4$	$-2.9\times10^5\pm5\times10^4$	$2\times10^3\pm1\times10^3$
2016-2018	*Full**		$6.7\times10^5\pm 1.8\times10^5$		
	*Outer***		$8.7\times10^4\pm4.5\times10^4$		
	North	$2.4\times10^5\pm8\times10^4$	$6.7\times10^4\pm5\times10^4$	$1.8\times10^5\pm3\times10^4$	$-1.1\times10^4\pm3\times10^3$
	South	$4.3\times10^5\pm1\times10^5$	$2.1\times10^5\pm5\times10^4$	$2.2\times10^5\pm5\times10^4$	$1\times10^3\pm1\times10^3$

**Full* is the sum of north and south net volumes (down to *DoC,* within black box on Fig. 6 and 7).
***Outer* is the sum of the morphological change beyond the morphological *DoC* (-14.5 m) and all areas outside of the area of the central embayment (beyond *DoC* and outside black box on Fig. 6 and 7).

4.3. Sub-tidal sediment redistribution

Both storm response and recovery was rather longshore-uniform (disregarding the increase in 3-dimensionality during the accretionary phases) in the inter-tidal zone, but less so in the sub-tidal region, warranting further investigation into the alongshore redistribution of sediment in especially the lower sub-tidal zone. The 6 *DoD*s covering the inner embayment recovery response (black dashed box down to the *DoC*, Fig. 2a) for the multi-annual erosive period 2011–2016, and inter-annual recovery period 2016–2018, are used to compute longshore variability and inter-annual volume change between the north and south (Fig. 9). The key finding here is that following the erosion over the 2011–2016 epoch, accretion of $0.5–2\times10^5$ occurred over each 6-month epoch in the recovery period, with most recovery occurring during the 2017/18 winter, especially in the sub-tidal region of the southern part of the beach.

Burvingt et al. (2017) defined longshore variation in the inter-tidal beach morphological response using the longshore variation index (*LVI*):

$$LVI = Q_{std}/(|Q_{mean}| + Q_{std}) \quad (1)$$

where Q_{std} is the standard deviation of the net volumetric change for cross-shore transects (Q_{cross}) and $|Q_{mean}|$ is the absolute value of the mean of Q_{cross} values. In order to discriminate between alongshore variability between the north and south sections and variability associated to 3-dimensionality, Q_{cross} is computed using 2-m alongshore-averaged cross-shore profiles, and is low-pass filtered using a moving averaged filter with a 400-m span. LVI index is then computed for the original and the filtered Q_{cross}. This index is dimensionless and varies between 0 and 1, with zero values implying cross-shore sediment transport is dominant, and $LVI = 1$ representing both significant alongshore transport and large 3-dimensionality. Hence, by applying the low-pass filter to Q_{cross}, most of the differences associated to the small scale morphology are eliminated. For 5 of the 6 epochs, *LVI* (both filtered and no filtered) for the sub-tidal region is considerably larger (LVI = 0.5–0.9) than for the inter-tidal region (LVI = 0.1–0.7), indicating that the sub-tidal is characterised by a significant longshore variability whereas the inter-tidal is more longshore-uniform. The only exception is the winter 2017/18 period during which the large LVI results from very significant changes in the lower inter-tidal bar/rip morphology (still present in the filtered signal), which is associated with the positive feedback between rip-cell circulation, sand transport and evolving bathymetry, and not driven by longshore transport processes.

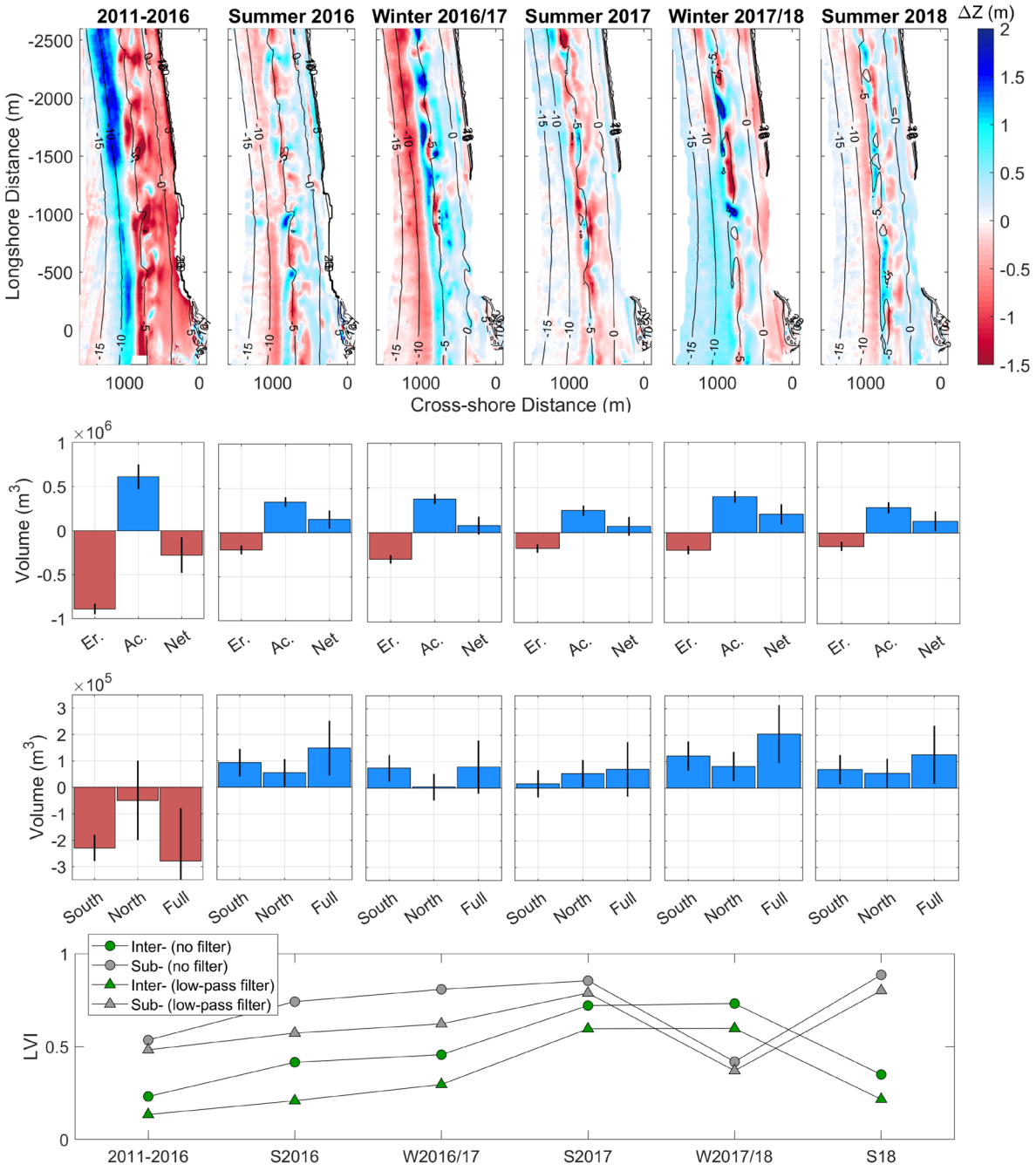

Fig. 9. Upper panels: 3D variability of Perranporth full embayment where red indicates erosion and blue erosion. Contours are from the first of the beach surveys. In order from 2nd to 3rd row panels: full embayment erosion (Er.), accretion (Ac.) and net (Net) volumetric change; and volumes for north and south sectors. All volumes are for epochs 2011–2016 and seasonal 2016–2018. Bottom panels: longshore variation index (*LVI*) computed using 2-m alongshore-averaged cross-shore profiles (circle) and a low-pass filter with a 400-m span (triangle).

5. Relating wave forcing and morphological change

To determine the sediment budget for any coastal domain, it is necessary to understand the forcing controls on sediment fluxes within, and in and out of the system, with waves being the primary forcing control in this instance. In the study area, the wave climate is strongly seasonal (Fig. 3f), such that the larger waves over winter periods are also slightly more northward in direction. Therefore, winters are associated with greater absolute wave power (forcing offshore transport), but also with greater southward alongshore wave power, likely to result in southward alongshore transport.

The wave parameters we seek to correlate with observed morphological change are the demeaned cumulative total wave power (P_{cum}) and the cumulative alongshore wave power ($P_{y,cum}$), computed for the 11-year available time series (2007–2018). The wave time series is transformed from the wave buoy location (~20 m depth ODN) to the breaking point using Van Rijn (2014). Assuming that beaches have an equilibrium condition related to the long-term mean wave forcing, total wave power is parameterised using the cumulative integral of the demeaned value (Stokes et al., 2016), denoted P_{cum}, as:

$$P_{cum}(n) = \int_{t_0}^{t_n} (P - \bar{P}) dt \quad (2)$$

where $\bar{P}$ is the long-term mean condition, and P corresponds to instantaneous wave power at the breakpoint. The assumption of equilibrium (or near-equilibrium) is supported by the morphology observations that show large variations but no clear trend on a decadal timescale (Fig. 5).

For alongshore wave power ($P_{y,cum}$), rather than demeaning the signal we select the long-term average power direction as shore-normal (285° in this instance), noting that the average wave direction is 283°, but bigger waves are more northerly. Again, the assumption here is that a long-term embayment equilibrium exists around variations in longshore forcing. The direction 285° also coincides with the mean orientation of the shoreline near the mid-point of the embayment, but this is not our primary motivation for choosing this angle.

$$P_{y,cum}(n) = \int_{t_0}^{t_n} P_{y,285}\, dt \quad (3)$$

For the purpose of relating wave forcing to morphologic change, only the southern sector observations are sufficiently long to draw statistical correlations (Fig. 5), therefore all analyses in this section are restricted to the southern part of the embayment. We seek to differentiate between forcing controls on the inter-tidal and sub-tidal components of the system, as observations suggest these systems behave, to some degree, independently (Fig. 5c-d). The morphologic change variables we will use for comparison to wave power are: (i) south-end inter-tidal volume, as it is the longest consistent time series [monthly 2007-2018]; (ii) south-end sub-tidal volume [sporadically 2011-2016, quarterly 2016-2018]; and (iii) total volume for the south end [time points as per sub-tidal volume]. Our preference is for analysis of the longest available dataset in each instance, to avoid misleading correlations with shorter time series'.

An initial examination of the correlations with sub-tidal volumes (Table 3, $V_{S,SUB}$) suggest this variable is poorly correlated with wave forcing. This may be due to the sub-tidal being open to flux from the inter-tidal as well as to beyond the outer boundaries, obscuring forcing correlations. What is required is for the exchange with the inter-tidal be offset from the sub-tidal volume. The value we are interested in is flux from the sub-tidal to beyond the outer boundaries (cross- and alongshore) of the southern sector, which is approximated by changes in the total system volume:

$$V_{S,TOTAL} = V_{S,SUB} + V_{S,INTER+DUNES} \quad (4)$$

We use the change in total south sector volume ($\Delta V_{S,TOTAL}$) as a proxy indicator for transport in and out of the sub-tidal outer domain boundaries. If we assume that sediment entering and leaving the southern sector primarily passes through the sub-tidal, then the total volume change ($\Delta V_{S,TOTAL}$) is the flux through the outer boundaries (offshore and lateral) of the sub-tidal region. For example, if over a given period $\Delta V_{S,INTER+DUNES}$ erode (-100 m^3/m) and $\Delta V_{S,SUB}$ also erodes (-100 m^3/m), then we assume that the sub-tidal gained +100 m^3/m from the inter-supratidal and therefore lost (-200 m^3/m) through the outer boundaries. This is not an ideal assumption as some material may be transported alongshore through the inter-tidal, but earlier findings have demonstrated the inter-tidal behaves coherently throughout the embayment and is largely cross-shore dominated (for example see Fig. 5c–e).

Considering the relationship between total and alongshore wave power (Fig 10a), there is a clear visual inverse correlation between P_{cum} and $P_{y,cum}$ at a seasonal time scale i.e., larger waves

are more northerly (see also Fig. 3f). However, at decadal time scales (2007-2018) there is no clear correlation, in fact the relationship is very weakly positive (Table 3; r = 0.2), suggesting that decadal trends in wave height are decorrelated from changes in wave direction. Inter-tidal morphological response ($V_{S,INTER}$; Fig. 10-second row) is negatively correlated with P_{cum} (Table 3; r = -0.59), indicating that more powerful waves erode the inter-tidal region. This relationship is consistent with the approach of a shoreline prediction model (Davidson et al., 2010; Splinter et al., 2014), which demonstrated a strong relationship at Perranporth between the shoreline position and disequilibrium in the dimensionless fall velocity parameter.

The southern total volume ($V_{S,TOTAL}$; red line in Fig. 10c-d) is inversely correlated with total wave power (r = -0.56, Fig. 10c) and positively correlated with alongshore wave power (r = 0.41, Fig. 10d). This suggests that as wave power increases overall and becomes cumulatively more negative (southward), the south end erodes, which is primarily attributed to flux through the sub-tidal boundaries. This is counter-intuitive, given that in a closed embayment, we would expect more northerly waves to drive clock-wise rotation and accrete the southern end of the embayment. Following the discussion by Harley et al. (2015), we also note that it is difficult to differentiate between the influence of total- and alongshore wave power on the total volume, as the wave variables themselves are correlated at short time scales (seasonal), and the strength of the correlations are sensitive to statistical design (e.g., start and end points of wave time series, shore-normal angle chosen). Additionally, low temporal resolution of the survey data aliases the seasonal signal. Taking these caveats into account, there appears to be a weak-moderate relationship where $V_{S,TOTAL}$ erodes during big, northerly waves (both for individual winters and multiple years above average wave power).

Assessing morphological correlations, it is interesting to note that the total southern system volume ($V_{S,TOTAL}$) is *positively* correlated (Table 3) with both $V_{S,INTER}$ (0.66) and $V_{S,SUB}$ (0.70), such that each contributes about half the total variance, indicating that conditions which cause the inter- or sub-tidal to erode (accrete), will also cause the total system to erode (accrete), primarily through transport beyond the outer boundaries. More broadly, the positive correlation between the inter-tidal and total volume suggests that the ability to predict inter-tidal volume change (e.g., using a shoreline prediction model such as Davidson et al., 2010) may also provide some skill in predicting total embayment volume, with the implication that total embayment volume may

respond to a disequilibrium in the wave climate, analogous to the inter-tidal. As mentioned in section 3, it is surprising to note that the expected inverse correlation between $V_{S,INTER}$ and $V_{S,SUB}$ is entirely absent at a time-lag of 0. Instead, it appears that these systems operate with a time-lag of approximately 1-year, with a peak cross-correlation of $r = 0.67$ found at 11.5-months lag (with the sub-tidal response following the inter-tidal). This suggests that sub-system response occurs at different timescales in reply to different forcing conditions. A hypothesised sequence to explain the lag in response may include: (i) an extreme storm that transports beach material far offshore, beyond the level of detectable change [inter-tidal erodes, sub-tidal is relatively unchanged]; (ii) an initial stage of recovery where sediment is transported mainly from the inner-sub-tidal to the beachface [inter-tidal accretes, sub-tidal erodes]; and (iii) a later phase of gradual transport from the lower-subtidal [from beyond the level of detectable change] to the upper-sub-tidal [inter-tidal unchanged, sub-tidal accretes]. The exact nature of this relationship is unclear and will be the target of future work.

Table 3. Correlation coefficients (*r*) for Perranporth southern sector beach volume and cumulative wave power (total and alongshore). Bold values are significant (*p-value* < *0.01*).

	P_{cum}	$P_{y,cum}$	$V_{S,\ INTER}$	$V_{S,\ SUB}$	$V_{S,TOTAL}$
P_{cum}	1	**0.2**	**-0.59**	-0.17	**-0.56**
$P_{y,cum}$		1	**0.24**	0.05	**0.41**
$V_{S,\ INTER}$			1	0.01	**0.66**
$V_{S,\ SUB}$				1	**0.70**
$V_{S,TOTAL}$					1

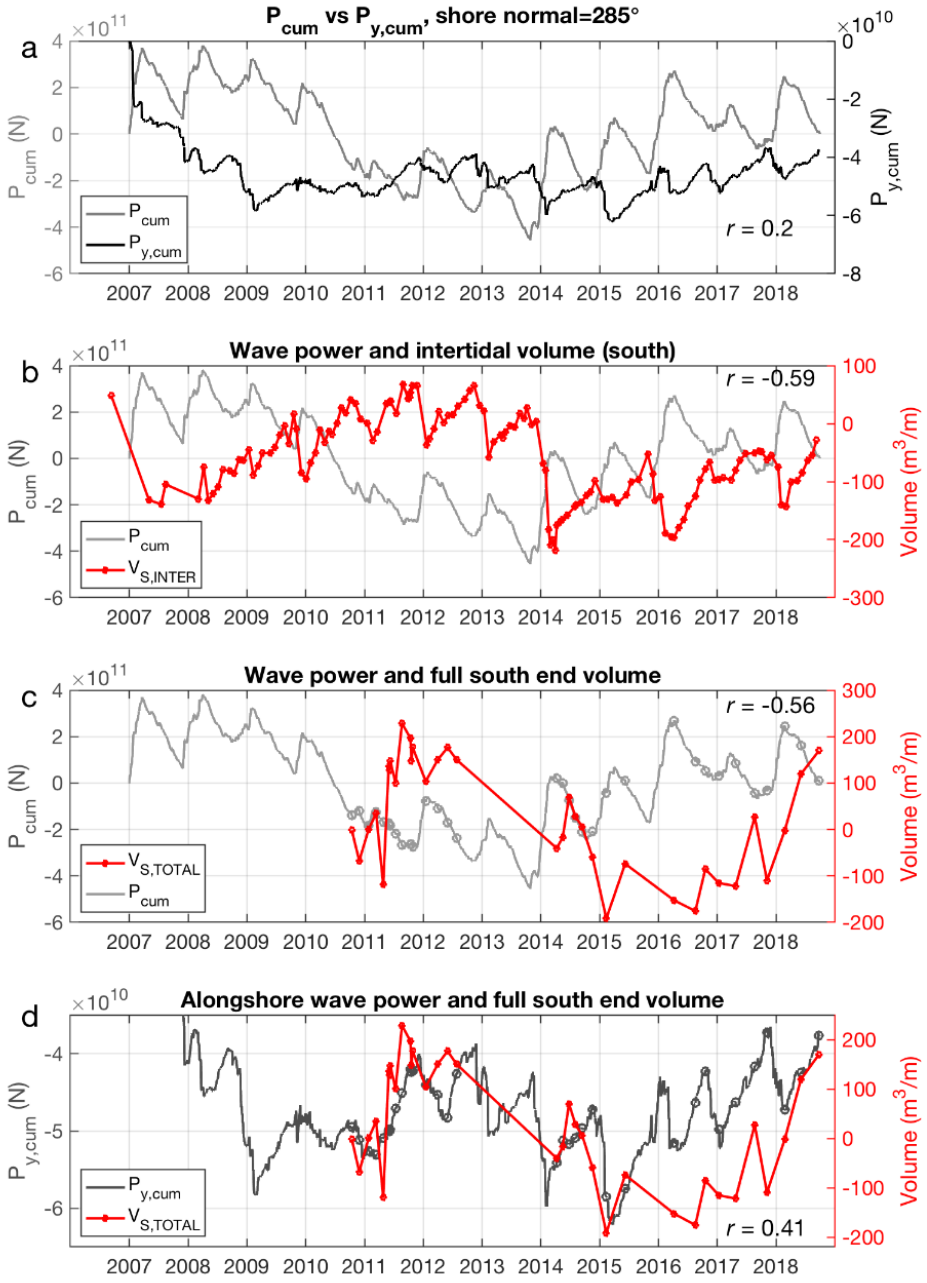

Fig. 10. Time series of wave power and volume observations. (a) P_{cum} and $P_{y,cum}$; (b) P_{cum} and $V_{S,INTER}$; (c) P_{cum} and $V_{S,TOTAL}$; (d) $P_{y,cum}$ against $V_{S,TOTAL}$. For (c, d) grey circles are the points on wave power time series' interpolated to volume. Southward alongshore wave power is negative.

6. Discussion

6.1. Sediment budget conceptual model

This study has demonstrated that, with reference to Fig. 1, Perranporth is an *open* system, that does not have a balanced sediment budget at the short to medium temporal scale (up to 10 years), and displays multi-annual accretional or erosional trends (Fig. 5e). Computed *DoDs* based on full embayment observations show significant morphological change in front of the headland bases and beyond the *DoC* in some sectors (Figs. 8 and 9). The alongshore continuity of the *DoC* contour line off the headland base (620 m in the south and 170 m in the north), linked with the detected morphological change beyond the inner embayment limits, suggests that Perranporth beach is part of an extended coastal cell. In line with earlier works (e.g., McCarroll et al., 2018; King et al., 2019; Valiente et al., 2019), these major morphological changes evidence substantial transport at depths > 15 m that are related to headland bypassing mechanisms.

A semi-quantitative conceptual sediment budget model that is consistent with all observations presented thus far is shown in Fig. 11. Volume changes in the north and south sectors ($\Delta V_N, \Delta V_S$) and fluxes within the model domain ($q_{x,N}$, $q_{x,S}$) are based on observations. We are unable to quantitatively resolve fluxes beyond the survey domain; instead, we refer to a prior numerical modelling study predicting bypass at the northern headland of Perranporth (McCarroll et al., 2018). That study predicted that rapid southward sediment flux occurred at the northern headland during winters (up to 0.5×10^5 m^3 for a single winter), whilst gradual northward transport (~0.2×10^5 m^3) occurred during 'summer' (spring to autumn). McCarroll et al. (2018) estimated transport through a transect extending off the northern headland, while in the present study the outer boundary for the northern sector extends cross-shore from the shoreline, and alongshore over the northern extent of the bay. Consequently, there are differences between the values inferred here and the values provided in McCarroll et al. (2018). The proposed flux values should be considered as broad estimates, useful for conceptualization and providing hypotheses for future testing, but they are not definitive. The direction and approximate magnitude of Q_N is inferred based on McCarroll et al. (2018), then the budget is balanced (Equations in Fig. 11) to calculate fluxes at the mid-point of the embayment (Q_M) and the southern boundary (Q_S), which are consistent with the observed morphologic change ($\Delta V_N, \Delta V_S$). Note that fluxes at the outer

boundaries (Q_N, Q_S) refer to both cross- and alongshore contributions. In summary, major phases of morphologic change include:

1. The **inter-tidal** erodes under energetic (and more northerly) waves and accretes when wave conditions are below average. This process is fairly uniform alongshore over the multi-year epochs (2011–2016; 2016–2018), but does vary for individual seasons (e.g., Fig. 11, Winter 2017–18).

2. During the **storm epoch** (2011–2016, Fig. 11), under larger and more northerly waves, the full embayment erodes, with the south eroding more than the north. Evidence is equivocal as to whether net transport is northward or southward, therefore we hypothesise two scenarios, to be resolved by future modelling efforts. In the first scenario (Fig. 11, Residual N transport), a net input of $1x10^5$ m^3 is estimated at the southern boundary (Q_N), with the northern sector losing sediment offshore and northward in the outer-subtidal. In the second scenario (Fig. 11, Residual S transport), a net input is estimated at the northern boundary, which implies that offshore sediment transport is occurring at the south end, exporting sediment beyond the survey region (Fig. 6).

3. During the **recovery period** (2016–2018), the waves are relatively smaller and more westerly, and the full embayment accretes. The south accretes more than the north, in particular during winter conditions. Northerly transport is inferred to occur during summer periods (Fig. 11, Summer 2016), assisted by a northerly residual tidal current (McCarroll et al., 2018). Influx is inferred to occur at both ends of the embayment during 'recovery winters' (Fig. 11, Winter 2017/18), demonstrating the critical role of winter wave conditions in multi-annual beach recovery (Burvingt et al., 2018; Dodet et al., 2019). This convergent flux is consistent with modelled circulation (McCarroll et al., 2018) for storms from the WNW (~285°), that may produce a northward current at the south end, and a southward current at the north end.

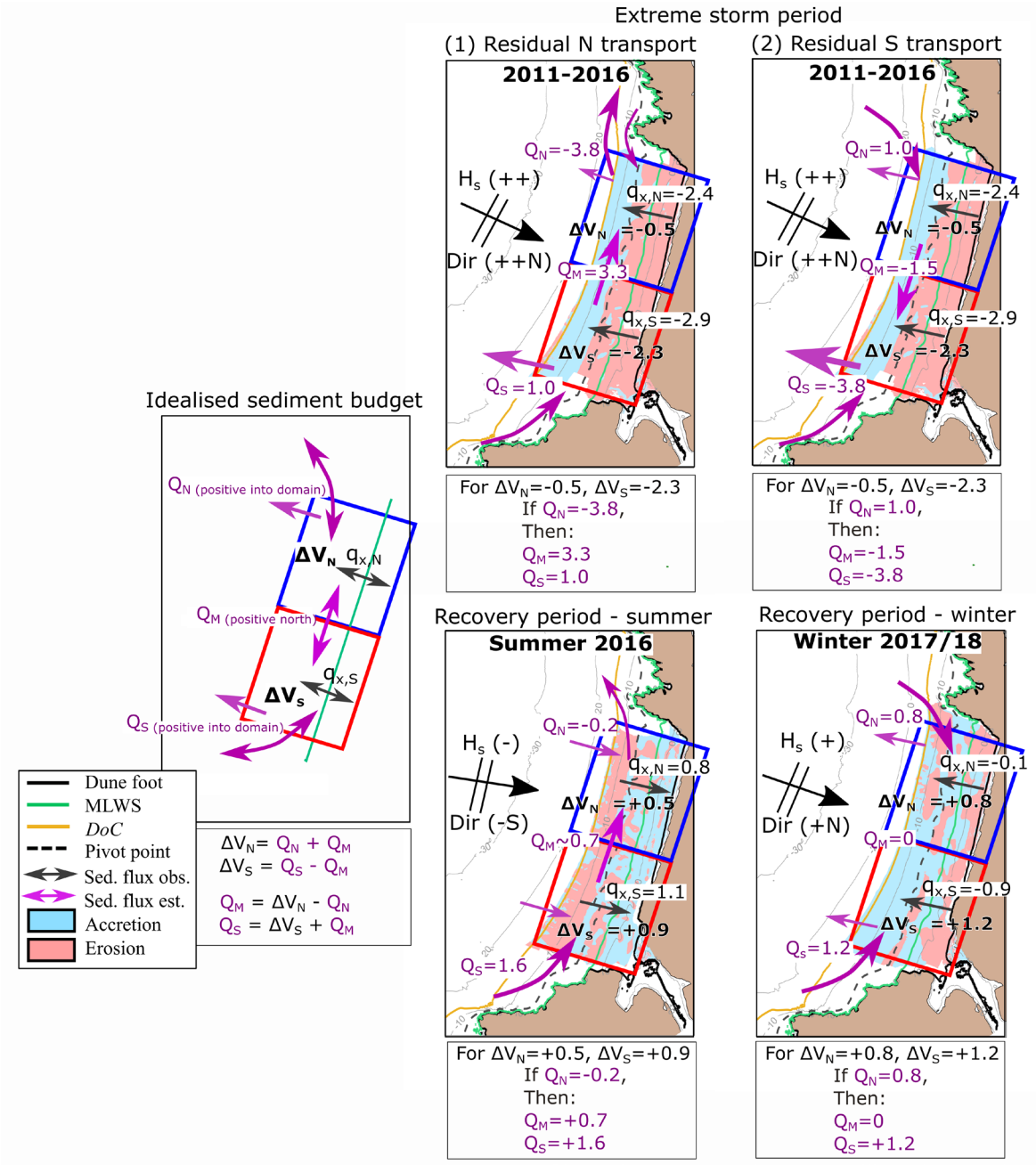

Fig. 11. Semi-quantitative conceptual sediment budget for Perranporth embayment with volume changes ($\Delta V_N, \Delta V_S$) and cross-shore flux ($q_{x,N}$, $q_{x,S}$; sed. flux obs.) based on observations. The external flux (Q_S, Q_N) refer to both cross- and alongshore contributions. Q_S and Q_M are estimated using observations and bypass rate in the northern headland (sed. flux est.). Flux and volume change values are x10^5 m^3. + and – symbols refer to magnitude of significant wave height (H_s) with (++) for large waves, (-) for low energy wave conditions and (+) for moderate to energetic conditions. Direction (*Dir*) refers to shore normal wave direction (*Dir* ~ 283°) with -S for more southward wave approach (W), and +N to ++N for WNW and NW, respectively.

The conceptual model (Fig. 11) is useful for explaining the observations, but currently has limited predictive capacity due the complexity of the system response. Further development through numerical modelling approaches are required in order to better predict sediment pathways.

6.2. Multi-annual embayment scale dynamics

The 'classic' characterization of beaches such as Perranporth is that winter storms erode the dunes and the upper part of the beach, depositing the sediment in sub-tidal bar systems, while calmer conditions return the sub-tidal sediment back to the beach (Komar, 1998). This is indeed what our understanding was for the studied beach based on almost a decade of inter-tidal beach surveys and a few sub-tidal surveys (Masselink et al., 2014; Scott et al., 2016), and which has led to the suggestion that Perranporth beach, and similar beaches in the region, are 'closed systems' (cf. Fig. 1-left panel). However, this characterization has shown to be incorrect as the full sediment budget analysis presented here indicates an 'open system' with sediment inputs and outputs in the order of 300 m^3 m^{-1} over a decadal time period (Fig. 5e). The inner embayment region seems therefore connected via sediment pathways to the region beyond the *DoC* and the bounding headlands, which is in line with numerical modelling by Valiente et al. (2019).

To explain the sediment pathways and close the sediment budget, it is necessary to consider both longshore sediment transport gradients along the embayment (Fig. 11) and from adjacent bays through headland bypassing. Importantly, the large sediment volumetric variations across the lower shoreface, which are of the same order of magnitude as those occurring in the inter-tidal region (c. 200 m^3 m^{-1}), is suggestive of an energetic longshore transport system across this deeper region, and it is possible that this transport system extends along the whole north coast of SW England as alluded to by May and Hanson (2003) and Valiente et al. (2019). These findings are critical for informing the next stages of regional scale modelling and observational studies and may lead to a shift in understanding of sediment budgets along exposed and macrotidal embayments globally.

There is an interesting contradiction that, despite the extensive sediment volumetric variations in the sub-tidal region (Fig. 5e), a model based solely on inter-tidal beach volume variations such as presented in Fig. 5c can be used to predict shoreline position over the 10-year time period (e.g., Davidson et al., 2010). This suggests that the upper part of the beach (supra-inter- and shallow sub-tidal) is partially decoupled from the deeper sub-tidal region. The vast

majority of beach studies in the past (and present) have been (and are) solely based on inter-tidal topographic surveys (e.g., Castelle et al., 2015; Loureiro et al., 2015; Masselink et al., 2016a,b; Harley et al., 2017; Burvingt et al., 2018; Mentaschi et al., 2018); however, full embayment surveys, such as pioneered here, are likely to reveal an additional layer of complexity concerning nearshore sediment transport and beach morphodynamics. Future numerical modelling efforts will be aimed at providing complementary understanding of embayment scale sediment fluxes.

7. Conclusions

- A total sediment budget approach was implemented across the macrotidal, high energy Perranporth embayment for the period 2011–2018, using a multi-method surveying approach and accounting for measurement uncertainties.

- Inter-tidal volumetric changes indicate a longshore coherent, cross-shore dominant behavior, following a seasonal cycle superimposed by a multi-annual oscillation induced by extremely energetic winter seasons, with full recovery taking at least 5 years.

- Total embayment (combined inter- and sub-tidal) volumes varied by c. 300 m^3 m^{-1} over 7-years, indicating that the inner embayment (down to the *DoC*) is 'open' and 'unbalanced' over multi-annual timescales.

- Sediment volumetric variations in the inter-tidal region are uncorrelated with those in the sub-tidal region at zero time-lag, but a positive correlation is observed at 1-year time-lag. This suggests that the upper and lower shoreface are partially decoupled, responding to different forcing controls.

- The largest dunes system monitored (northern Perranporth) experienced a significant erosion event in 2013/14 (15 m onshore translation of dune foot) with little recovery within 5 years.

- Inter-tidal sediment volume for the long-term southern sector time series was inversely correlated with variations in total wave power (r = -0.6), coherent with a cross-shore dominated response. Total sediment volume change (primarily due to flux through the outer sub-tidal boundary) was correlated with both total (r = -0.6) and alongshore wave power (r = 0.4), suggesting a combined cross- and alongshore dominated response.

- The inter-tidal volume was found to be positively correlated with the total volume (for the south sector), such that when the inter-tidal eroded or accreted, so too did the total system. This was evident for an erosive period of extreme waves (2011–2016), followed by a 'recovery' period (2016–2018), where consistent influxes into the embayment were observed, even during energetic winter periods. This suggests a degree of equilibrium for the total embayment volume.

- A conceptual model was presented that balances the observed volume changes with inferred fluxes, forced by variations in total and alongshore wave power. At present, this model has limited predictive capacity and requires further development through numerical modelling approaches to better predict future sediment budgets on similar coastlines.

- Given the extent of flux through the sub-tidal outer boundaries, it is likely that Perranporth and beaches on similar coastlines form part of an extended coastal cell, with individual embayments linked via a 'river of sand' that flows around headlands.

Acknowledgments

This work was supported by UK Natural Environment Research Council grant (NE/M004996/1; BLUE-coast project). This study is only possible thanks to the efforts of the members of the Coastal Process Research Group who have been, and still are, collecting observations at Perranporth. Special thanks to Aaron Barret, Peter Ganderton, Richard Kenyon, Oliver Bilson, Olivier Burvingt and Erin King for supporting the many field efforts during the last years. The Channel Coastal Observatory is project stakeholder and kindly provided LiDAR data. We would also like to acknowledge QPS for their ongoing support with multi beam software provision (QINSy/Qimera/FMGT).

References

Aagaard, T. (2011). Sediment transfer from the beach to shoreface: The sediment budget of an accreting beach on the Danish North Sea Coast. *Geomorphology* 135, 143–157.

Bowen, A.J., Inman, D.L. (1966). Budget of Littoral Sand in the Vicinity of Point Arguello, California. U.S. Army Coastal Engineering Research Center, *Technical Memorandum No. 19*, 56p.

Brasington J., Langham J., Rumsby B. (2003). Methodological sensitivity of morphometric estimates of coarse fluvial sediment transport. *Geomorphology* 53(3–4), 299–316. DOI: 10.1016/S0169-555X(02)00320-3

Brasington, J., Rumsby, B.T., Mcvey, R.A. (2000). Monitoring and modelling morphological change in a braided gravel-bed river using high resolution GPS-based survey. *Earth Surface Processes and Landforms* 25(9): 973–990.

Burvingt, O., Masselink, G., Russell, P., Scott, T. (2017). Classification of beach response to extreme storms. *Geomorphology* 295, 722–737.

Burvingt, O., Masselink, G., Scott, T., Davidson, M., Russell, P. (2018). Climate forcing of regionally-coherent extreme storm impact and recovery on embayed beaches. *Marine Geology* 401, 112–128.

Calder, B.R., Mayer, L.A. (2003). Automatic processing of high-rate, high density multi-beam echosounder data. *Geochemistry, Geophysics, Geosystems* 4(6): 1048. DOI: 10.1029/2002GC000486.

Calder, B.R., Wells, D. (2007). CUBE User's Manual – Version 1.14. University of New Hampshire, USA.

Caldwell, J.M. (1966). Coastal processes and beach erosion. *Journal of the Society of Civil Engineers*, 53 (2), 142–157.

Castelle, B., Bujan, S., Ferreira, S., Dodet, G. (2017b). Foredune morphological changes and beach recovery from the extreme 2013/2014 winter at a high-energy sandy coast. *Marine Geology* 385, 41–55.

Castelle, B., Dodet, G., Masselink, G., Scott, T. (2018). Increased Winter-Mean Wave-Height, Variability, and Periodicity in the Northeast Atlantic over 1947-2017. *Geophysical Research Letters* 45(2). DOI: 10.1002/2017GL076884

Castelle, B., Marieu, V., Bujan, S., Splinter, K.D., Robinet, A., Sénéchal, N., Ferreira, S. (2015). Impact of the winter 2013–2014 series of severe Western Europe storms on a double-barred sandy coast: beach and dune erosion and megacusp embayments. *Geomorphology* 238, 135–148.

Church, J.A., White, N.J. (2011). Sea-level rise from the late 19th to the early 21st Century. *Surveys in Geophysics* 32, 585–602. DOI: 10.1007/s10712-011-9119-1.

CIRIA (1996). Beach management manual. CIRIA Report 153.

Coastal Engineering Research Center (1984). *Shore Protection Manual, Volume I*. Department of the Army Waterways Experiment Station, Coprs of Engineers, Vicksburg, Mississippi, pp. 652.

Coco, G., Senechal, N., Rejas, A., Bryan, K., Capo, S., Parisot, J.P., Brown, J.A., MacMahan, J.H.M. (2014). Beach response to a sequence of extreme storms. *Geomorphology* 204, 493–501.

Cowell, P.J, Stive, M.J.F., Niedoroda, A.W., Swift, D.J.P., de Vriend, H.J., Buijsman, M.C., Nicholls, R.J., Roy, P.S., Kaminsky, G.M., Cleveringa, J., Reed, C.W., de Boer, P.L. (2003). The Coastal-Tract (Part 2): Applications of Aggregated Modeling of Lower-order Coastal Change. *Journal of Coastal Research* 19(4), 828–848.

Cudaback, C.N., Washburn, L., Dever, E. (2005). Sub-tidal inner-shelf circulation near Point Conception, California. *Journal of Geophysical Research: Oceans* 110, C10007. doi:10.1029/2004JC002608

Davidson, M.A., Lewis, R.P., Turner, I.L. (2010). Forecasting seasonal to multi-year shoreline change. *Coastal Engineering* 57, 620-629.

Dodet, G., Castelle, B., Masselink, G., Scott, T., Davidson, M., Floc'h, F., Jackson, D., Suanez, S. (2019). Beach recovery from extreme storm activity during the 2013/14 winter along the Atlantic coast of Europe. *Earth Surface Processes and Landforms*, 44(1), 393-401. George, D.A., Largier, J.L., Storlazzi, C.D., Barnard, P.L. (2015). Classification of rocky headlands in California with relevance to littoral cell boundary delineation. *Marine Geology 369*, 137–152.

Guisado-Pintado, E., Jackson, D.W.T. (2018). Multi-scale variability of storm Ophelia 2017: The importance of synchronised environmental variables in coastal impact. *Science of Total Environment* 630, 287–301.

Harley, M.D., Turner, I.L., Kinsela, M.A., Middleton, J.H., Mumford, P.J., Splinter, K.D., Phillips, M.S., Simmons, J.A., Hanslow, D.J., Short, A.D. (2017). Extreme coastal erosion enhanced by anomalous extratropical storm wave direction. *Sci. Rep*. 7 (6033). https://doi.org/10.1038/s41598-017-05792-1.

Harley, M.D., Turner, I.L., Short, A.D. (2015). New insights into embayed beach rotation: the importance of wave exposure and cross-shore processes. *J. Geophys. Res. Earth Surf* 120, 470-1484. https://doi.org/10.1002/2014JF003390.

Herbich, J.B. (2000). *Handbook of Coastal Engineering*. McGraw-Hill Professional, New York City, USA.

Inman, D.L., Frautschy, J.D. (1966). Littoral processes and the development of shorelines. *Proceeding Coastal Engineering Specialty Conference*, Reston, VA, ASCE, pp. 511-536.

King, E., Conley, D., Masselink, G., Leonardi, N., McCarroll, R.J., Scott, T. (2019). The Impact of Waves and Tides on Residual Sand Transport on a Sediment-poor, Energetic and Macrotidal Continental Shelf. *Journal of Geophysical Research Ocean* (in press.).

Kinsela, M.A., Morris. B.D., Linklater, M., Hanslow, D.J. (2017). Second-pass asessment of potential exposure to shoreline change in New South Wales, Australia, using a sediment compartments framework. *Journal of Marine Science and Engineering* 5, 61. DOI: 10.3390/jmse5040061

Komar, P.D. (1998). *Beach processes and sedimentation*. Prentice-Hall, Inc., Simon & Schuster, Upper Saddle River, NJ, pp. 66–72.

Lane S.N. (1998). The use of digital terrain modelling in the understanding of dynamic river channel systems. In *Landform Monitoring, Modelling and Analysis*, Lane SN, Richards K, Chandler J (eds). Wiley: Chichester; 311–342.

Lane, S.N., Chandler, J.H., Richards, K.S. (1994). Developments in monitoring and modeling small-scale river bed topography. *Earth Surface Processes and Landforms* 19(4): 349–368. DOI: 10.1002/esp.3290190406.

Lane, S.N., Westaway, R.M., Hicks, D.M. (2003). Estimation of erosion and deposition volumes in a large, gravel-bed, braided river using synoptic remote sensing. *Earth Surface Processes and Landforms* 28(3): 249–271. DOI: 10.1002/esp.483.

Loureiro, C., Ferreira, Ó., Cooper, J. A. G. (2012). Extreme erosion on high-energy embayed beaches: influence of megarips and storm grouping. *Geomorphology* 139, 155–171.

Masselink, G., Austin, M., Scott, T., Poate, T., Russell, P. (2014). Role of wave forcing, storms and NAO in outer bar dynamics on a high-energy, macro-tidal beach. *Geomorphology* 226, 76–93.

Masselink, G., Castelle, B., Scott, T., Dodet, G., Suanez, S., Jackson, D., Floc'h, F. (2016a). Extreme wave activity during 2013/2014 winter and morphological impacts along the Atlantic coast of Europe. *Geophysical Research Letters* 43 (5), 2135–2143.

Masselink, G., Scott, T., Poate, T., Russell, P., Davidson, M., Conley, D. (2016b). The extreme 2013/2014 winter storms: hydrodynamic forcing and coastal response along the southwest coast of England. *Earth Surface Processes and Landforms* 41 (3), 378–391.

Masselink, G.; Short, A.D. (1993) The effect of tide range on beach morphodynamics and morphology: A conceptual beach model. *J. Coast. Res.*, *9*, 785–800.

May, V.J., Hansom, J.D. (2003). *Coastal Geomorphology of Great Britain*, Geological edition. Joint Nature Conservation Committee, Peterborough, pp. 754.

McCarroll, J., Masselink, G., Valiente, N. G., Scott, T., King, E. (2018). Wave and tidal controls on headland bypassing and embayment circulation. *Journal of Marine Science and Engineering* 6 (3), 94. https://doi.org/10.3390/jmse6030094.

Mentaschi, L., Vousdoukas, M.I., Pekel, J., Voukouvalas, E., Feyen, L. (2018). Global long-term observations of coastal erosion and accretion. Scientific Reports 8, 12876. https://doi.org/10.1038/s41598-018-30904-w

Milne, J.A., Sear, D. (1997). Modelling river channel topography using GIS. *International Journal of Geographical Information Science* 11(5), 499–519. DOI: 10.1080/136588197242275.

Plant, N.G., Holland, K.T, Puleo, J.A. (2002). Analysis of the scale errors in nearshore bathymetric data. *Marine Geology* 191(1–2), 71–86.

Poate, T., Masselink, G., Russell, P., Austin, M. (2014). Morphodynamic variability of high-energy macrotidal beaches, Cornwall, UK. *Mar. Geol.* 350, 97–111.

Prodger, S., Russell, P., Davidson, M. (2017). Grain-size distributions on high-energy sandy beaches and their relation to wave dissipation. *Sedimentology* 64, 1289–1302.

Rosati, J.D. (2005). Concepts in sediment budgets. *Journal of Coastal Research* 21, 307–322.

Schimel, A.C.G., Ierodiaconou, D., Hulands, L., Kennedy, D.M. (2015). Accounting for uncertainty in volumes of seabed change measured with repeat multi-beam sonar surveys. *Cont. Shelf Res.* 111, 52–68. https://doi.org/10.1016/j.csr.2015.10.019.

Scott, T., Masselink, G., Austin, M.J., Russell, P.E. (2014). Controls on macrotidal rip current circulation and hazard. *Geomorphology* 214, 198–215 http://dx.doi.org/10.1016/j.geomorph.2014.02.005.

Scott, T., Masselink, G., O'Hare, T., Saulter, A., Poate, T., Russell, P., Davidson, M., Conley, D. (2016). The extreme 2013/2014 winter storms: Beach recovery along southwest coast of England. *Marine Geology* 382, 224–241.

Scott, T., Masselink, G., Russell, P. (2011). Morphodynamic characteristics and classification of beaches in England and Wales. *Marine Geology* 286 (1-4), 1–20.

Short, A.D. (1985). Rip-current type, spacing and persistence, Narrabeen Beach, Australia. *Marine Geology* 65(1-2), 47–71.

Short, A.D. (2010). Role of geological inheritance in Australian beach morphodynamics. *Coastal Engineering*, 57(2), 92–97.

Short, A., Masselink, G. (1999). Embayed and structurally controlled beaches. In Short, A. E., editor, *Handbook of Beach and Shoreface Morphodynamics*, pp. 230–249. John Wiley & Sons, Chichester.

Sibson, R. (1981). "A Brief Description of Natural Neighbor Interpolation," chapter 2. In *Interpolating Multivariate Data*. New York: John Wiley & Sons, 21–36.

Splinter, K.D., Carley, J.T., Golshani, A., Tomlinson, R. (2014). A relationship to describe the cumulative impact of storm clusters on beach erosion. *Coast. Eng.* 83, 49–55.

Stokes, C., Russell, P., Davidson, M. (2016). Sub-tidal and Inter-tidal Three-Dimensionality at a High Energy Macrotidal Beach. *Journal of Coastal Research* 75, (sp1) 472-476.

Taylor, J. (1997). *An Introduction to Error Analysis: the Study of Uncertainties in Physical Measurements,* 2nd edn. University Science Books: Sausalito, CA.

Thom, B.G., Eliot, I., Harvey, N., Rissik, D., Sharples, C., Short, A.D., Woodroffe, C.D. (2018). National sediment compartment framework for Australian coastal management. *Ocean and Coastal Management* 154, 103–120.

United Kingdom Hydrographic Office (2011). INSPIRE Portal & Bathymetry DAC. Available at http://aws2.caris.com/ukho/mapViewer/map.action

Valiente, N.G., Masselink, G., Scott, T., Conley, D., McCarroll, J. (2019). Evaluation of the role of waves and tides on depth of closure and potential for headland bypassing. *Marine Geology* 407, 60-75. https://doi.org/10.1016/j.margeo.2018.10.009

Van Rijn, L.C. (1997). Sediment transport and budget of the central coastal zone of Holland. *Coastal Engineering* 32, 61–90

Van Rijn, L.C. (2011). Coastal erosion and control. *Ocean & Coastal Management* 54(12), 867‑887.

Van Rijn, L.C. (2014). A simple general expression for longshore transport of sand, gravel and shingle, *Coastal Engineering* 90, 23‑39.

Vieira da Silva, G., Toldo, E.E., Klein, A.H.F., Short, A.D., Tomlinson, R., Strauss, D. (2017). A comparison between natural and artificial headland sand bypassing in Santa Catarina and the Gold Coast. *Australasian Coasts & Ports 2017: Working with Nature*, 1111.

Wiggins, M., Scott, T., Masselink, G., Russel, P., McCarroll, R.J. (2018). Coastal embayment rotation: response to extreme events and climate control, using full embayment surveys. *Geomorphology* 327, 385–403. https://doi.org/10.1016/j.geomorph.2018.11.014

Wise, S.M. (1998). The effect of GIS interpolation errors on the use of digital elevation models in geomorphology. In *Landform Monitoring, Modelling and Analysis*, Lane SN, Richards K, Chandler J (eds). Wiley: Chichester; 139–164.

Wechsler, S.P. (2003). Perceptions of digital elevation model uncertainty by DEM users. *URISA Journal* 15(2), 57–64.

Wechsler, S.P., Kroll, C.N. (2006). Quantifying DEM uncertainty and its effect on topographic parameters. *Photogrammetric Engineering and Remote Sensing* 72(9), 1081–1090.

Wheaton, J.M., Brasington, J., Darby, S.E., Sear, D.A. (2010). Accounting for uncertainty in DEMs from repeat topographic surveys: improved sediment budgets. *Earth Surface Processes and Landforms* 35, 136–156.